To appear in ApJ
Preprint typeset using LaTeX style emulateapj v. 11/12/01

2-D RADIATIVE TRANSFER IN PROTOSTELLAR ENVELOPES: I. EFFECTS OF GEOMETRY ON CLASS I SOURCES

Barbara A. Whitney[1], Kenneth Wood[2], J. E. Bjorkman[3], & Michael J. Wolff[1]
To appear in ApJ

ABSTRACT

We present 2-D radiation transfer models of Class I Protostars and show the effect of including more realistic geometries on the resulting spectral energy distributions and images. We begin with a rotationally flattened infalling envelope as our comparison model, and add a flared disk and bipolar cavity. The disk affects the spectral energy distribution most strongly at edge-on inclinations, causing a broad dip at about 10 μm (independent of the silicate feature) due to high extinction and low scattering albedo in this wavelength region. The bipolar cavities allow more direct stellar+disk radiation to emerge into polar directions, and more scattering radiation to emerge into all directions. The wavelength-integrated flux, often interpreted as luminosity, varies with viewing angle, with pole-on viewing angles seeing 2-4 times as much flux as edge-on, depending on geometry. Thus, observational estimates of luminosity should take into account the inclination of a source. The envelopes with cavities are significantly bluer in near-IR and mid-IR color-color plots than those without cavities. Using 1-D models to interpret Class I sources with bipolar cavities would lead to an underestimate of envelope mass and an overestimate of the implied evolutionary state. We compute images at near-, mid-, and far-IR wavelengths. We find that the mid-IR colors and images are sensitive to scattering albedo, and that the flared disk shadows the midplane on large size scales at all wavelengths plotted. Finally, our models produce polarization spectra which can be used to diagnose dust properties, such as albedo variations due to grain growth. Our results of polarization across the 3.1 μm ice feature agree well with observations for ice mantles covering 5% of the radius of the grains..

Subject headings: radiative transfer—stars: formation—stars: imaging— stars: pre-main sequence—circumstellar matter—dust, extinction— polarization

1. INTRODUCTION

Lada and collaborators first classified pre-main sequence stars into an evolutionary sequence, Class I through III, by the shapes of their spectra energy distributions (SEDs) (Lada 1987; Myers et al. 1987; Adams, Lada, & Shu 1987). Class I sources, the subject of this paper, are thought to be T Tauri stars surrounded by infalling envelopes. More recently, an earlier stage was proposed, the Class 0 stage to describe more deeply embedded sources (André, Ward-Thompson, & Barsony 1993). This called into question whether the Class I envelopes are merely remnant or are still collapsing, though detailed radiative transfer models of several Class I sources require substantial envelope mass (typically 10-20 times greater than a Class II disk), and suggest that the envelopes are still infalling, if at a less embedded stage than the Class 0 stage (Adams et al. 1987; Kenyon et al. 1993a,b; Whitney, Kenyon, & Gómez 1997; Stark et al. 2002).

Adams et al. (1987) successfully interpreted the SEDs of Class I sources with 1-D radiative transfer models of spherically-averaged rotationally-flattened infalling envelopes. Kenyon et al. (1993a) applied "1.5-D" radiative transfer calculations to model the SEDs of the Taurus Class I sources, using the spherically-averaged density for calculating the temperature. The average model infall rates and centrifugal radii were consistent with observed sound speeds and disk sizes. Efstathiou & Rowan-Robinson (1991) also performed accurate 2-D radiative transfer solutions using the rotationally-flattened infalling envelope. All of these SED models of Class I sources tend to have similar features, steeply rising at about 1 μm, then gradually rising to 100 μm, and falling off to 1000 μm (see Figure 9, top left panel for a similar model). More recently, Nakazato, Nakamoto, & Umemura (2003) calculated 2-D models of Class I objects which included a disk and a piece-wise spherically symmetric envelope divided into two latitude sectors, each having a radial power law independent of polar angle. To create a bipolar cavity, the density was lowered in the polar sector.

Most of the previous 1-D and even the 2-D SED models of Class I sources underestimate the optical/near-IR flux when compared to observations. Scattered light models (Kenyon et al. 1993b) showed that bipolar cavities are required to allow an escape path for the short-wavelength radiation, and to fit the extended images and polarization maps of these sources (Whitney et al. 1997, Lucas & Roche 1997, 1998). Gómez, Whitney, & Kenyon (1997) found [S II] emission from jets and Herbig-Haro objects in nearly all the Taurus Class I sources, providing a mechanism for producing the bipolar cavities. In addition, most of the Class I sources are known to have low-velocity molecular outflows (Moriarty-Schieven et al. 1992, 1995a,b; Chandler et al. 1996, Tamura et al. 1996, Hogerheijde et al. 1998). High spatial-resolution images

[1] Space Science Institute, 3100 Marine Street, Suite A353, Boulder, CO 80303; bwhitney@colorado.edu
[2] School of Physics & Astronomy, University of St Andrews, North Haugh, St Andrews, Fife, KY16 9AD, Scotland the Brave; kw25@st-andrews.ac.uk
[3] Ritter Observatory, MS 113, Department of Physics & Astronomy, University of Toledo, Toledo, OH 43606-3390; jon@physics.utoledo.edu

(Padgett et al. 1999) and scattered-light models (Stark et al. 2002) find that vertically extended disks, an expected consequence of rotational infall, are required in addition to the infalling envelopes to fit the images several Class I sources. The hydrodynamic collapse models of Bate (1998) also produce substantial disks in Class I sources.

Since it is clear from these studies that Class I sources have disks and cavities in addition to infalling envelopes, we wish to determine if these more complicated geometries give different SEDs than the previous models show. This paper computes the exact solutions for 2-D radiative transfer in Class I sources including the realistic geometrical effects of a rotationally flattened envelope, a flared accretion disk, and bipolar cavity. We find that both the disks and cavities have substantial effects on the resulting SEDs, especially in the mid-IR. These variations can be tested with new ground-based and upcoming space-based infrared observations. In addition to SEDs, we compute images and polarization. This paper details how the geometry affects the SED for a single evolutionary state, the Class I source. In a followup paper we will explore these effects in an evolutionary sequence. The next section describes the models, §3 shows the results of four different geometries, and §4 concludes with a discussion of the results.

2. RADIATIVE TRANSFER MODELS

2.1. *Ingredients of the Model: Disk, Envelope, & Cavity Structure*

We wish to use as realistic a geometry as possible to describe the Class I protostar. Since disks appear to be ubiquitous in star forming regions (Cohen, Emerson, & Beichman 1989; Strom et al. 1989; Beckwith et al. 1990, Dutrey, Guilloteau, & Simon 1994; Koerner & Sargent 1995; Saito et al. 1995; Burrows et al. 1996), and therefore the infalling envelope likely has angular momentum, we choose for the envelope geometry the infall solution that includes rotation (Ulrich, 1976, Cassen & Moosman 1981, Terebey, Shu, & Cassen 1984). On larger scales, magnetic fields (Galli & Shu 1993a,b, Li 1998, Ciolek & Königl 1998) and initial motions prior to dynamical collapse (Foster & Chevalier 1993) may affect the structure but within the infalling region, the effects of rotation likely dominate over magnetic effects. This region contributes most to the SED and images. The density structure for the rotationally-flattened infalling envelope within the infalling radius is given by:

$$\rho = \frac{\dot{M}_{\rm env}}{4\pi\left(GM_\star R_c^3\right)^{1/2}}\left(\frac{r}{R_c}\right)^{-3/2}\left(1+\frac{\mu}{\mu_0}\right)^{-1/2}\left(\frac{\mu}{\mu_0}+\frac{2\mu_0^2 R_c}{r}\right)^{-1} \quad (1)$$

where $\dot{M}_{\rm env}$ is the envelope mass infall rate, R_c is the centrifugal radius, $\mu=\cos\theta$ and μ_0 is the cosine polar angle of a streamline of infalling particles as $r\to\infty$). The equation for the streamline is given by

$$\mu_0^3+\mu_0(r/R_c-1)-\mu(r/R_c)=0\ . \quad (2)$$

For the disk structure, we use a standard flared accretion density (Shakura & Sunyaev 1973, Lynden-Bell & Pringle 1974; Pringle 1981; Bjorkman 1997; Hartmann 1998):

$$\rho=\rho_0\left[1-\sqrt{\frac{R_\star}{\varpi}}\right]\left(\frac{R_\star}{\varpi}\right)^{\alpha}\exp\left\{-\frac{1}{2}\left[\frac{z}{h(\varpi)}\right]^2\right\}\ , \quad (3)$$

where ϖ is the radial coordinate in the disk midplane and the scale height increases with radius, $h=h_0\,(\varpi/R_\star)^{\beta}$. For the models presented here, we adopt: $\beta=1.25$, $\alpha=2.25$, $h_0=0.01R_\star$, giving a scale height at the disk outer radius of $h[100\mathrm{AU}]=10\mathrm{AU}$. The β and α values are consistent with detailed hydrostatic structure calculations (D'Alessio et al. 1998). The exact disk structure in an object with an infalling envelope is likely to vary from this geometry, since the disks are accreting from the infalling envelope. However, observations and models of Class I sources show morphologies consistent with vertically extended disks (Padgett et al. 1999, Stark et al. 2002) so the flared disk seems to be a good starting point for this investigation. We include accretion energy, $d\dot{E}_{\rm acc}/dV$, in the disk using the $\alpha-$disk prescription (Shakura & Sunyaev 1973, Kenyon & Hartmann 1987, Bjorkman 1997; Hartmann 1998):

$$\frac{d\dot{E}_{\rm acc}}{dV}=\frac{3GM_\star\dot{M}_{\rm disk}}{\sqrt{32\pi^3}\varpi^3h(\varpi)}\left[1-\sqrt{\frac{R_\star}{\varpi}}\right]\exp\left\{-\frac{1}{2}\left[\frac{z}{h(\varpi)}\right]^2\right\}\ , \quad (4)$$

where the disk accretion rate, $\dot{M}_{disk}$ is given by

$$\dot{M}_{\rm disk}=\sqrt{18\pi^3}\,\alpha_{\rm disk}\,V_c\,\rho_0\,h_0^3/R_\star\ , \quad (5)$$

with the critical velocity $V_c=\sqrt{GM_\star/R_\star}$. For the disk parameters used in this paper (§3), Table 1 shows the resulting disk accretion rate and accretion luminosity. For simplicity, accretion energy inside the dust destruction radius, R_{dust}, is emitted with the stellar spectrum. Thus the accretion luminosity emitted within the dusty disk is

$$L_{\rm acc}=\frac{GM_\star\dot{M}}{2R_{\rm dust}}\left[3-2\sqrt{R_\star/R_{\rm dust}}\right]. \quad (6)$$

Since near-IR images of Class I sources require bipolar cavities to fit the observations (Kenyon et al. 1993b, Whitney et al. 1997), we include them in these models. We choose two shapes to describe the cavities since they both appear to be evident in observations (Padgett et al. 1999, Stark et al. 2002; Reipurth et al. 2000). These are a streamline, which is conical on large scales, and a curved cavity. The streamline cavity shape might occur if precessing jets carve out a conical shape while infalling material outside of the cavity continues to fall in along streamlines. The cause of a curved shape is less certain. The streamline cavity shape is defined by equation (2); at each (μ,r), μ_0 is calculated, and if it is greater than the chosen cavity angle, the density is set to the cavity density. Whitney & Hartmann (1993) show a picture of this cavity shape in their Figure 1. The curved cavity follows $z=a\varpi^b$, where $\varpi=\sqrt{x^2+y^2}$. We include a small amount of dust in the cavity with constant density, $n_{H2}=2\times10^4\mathrm{cm}^{-3}$, as expected for a cylindrical outflow. The density in the cavity may vary from $n_{H2}\sim10^3-10^6\mathrm{cm}^{-3}$ in the high- and low-velocity flow regions (Bachiller & Tafalla 1999; Reipurth & Raga 1999). A more realistic cavity density distribution including such large variations could have a substantial effect on the radiative transfer, and will be considered in future work. The total mass in the cavity, about $6 \times 10^{-3} M_{\odot}$, is similar to observed outflow masses in Taurus Class I sources (Moriary-Schieven et al. 1995b, Chandler et al. 1996, Hogerheijde et al. 1998).

2.2. *Radiation Transfer Method*

To calculate the radiative transfer, we incorporated the Monte Carlo radiative equilibrium routines developed by Bjorkman & Wood (2001) into a 3-D spherical-polar grid code (Whitney & Wolff 2001). Bjorkman & Wood tested their codes by comparing to a set of benchmark calculations developed by Ivezič et al. (1997) for spherically symmetric codes. They then applied their method to 2-D ellipsoidal envelopes and T Tauri disks (Wood et al. 2002a,b). These codes use a numerical optical depth integrator that operates on an analytically prescribed density. The numerical integrator has difficulty handling sharp density gradients. In order to include arbitrary density distributions, such as bipolar cavities or 3-D clumpy envelopes, we have developed a code that uses a 3-D spherical-polar grid (Whitney & Wolff 2001). The density is constant within a grid cell, allowing for straightforward integration of optical depth through the grid. Since the density in each cell is computed only once at the beginning of the processing, we can incorporate very complicated analytic density formulations, or use tabular densities derived from hydrodynamical simulations. For the protostellar envelope case, the grid has variable spacing in r and θ to sample the vastly different density variations and size scales from the inner disk region to the outer envelope. The radial spacing is logarithmic in the inner region of the disk, to resolve the inner edge of the disk in optical depth, and then follows a power-law spacing out to the edge of the envelope, chosen to be 5000 AU for the models presented here.

We include accretion in our disk, following Wood et al. (2002a). We also attach a diffusion solution to the inner regions (Bjorkman et al. 2003). We tested our grid code by comparing calculations of ellipsoidal envelopes and T Tauri disks to the 2-D codes of Bjorkman & Wood (2001) and Wood et al. (2002a,b). The results were identical.

In these models, the luminosity is produced by the central star and disk accretion; it then gets absorbed and reemitted, or scattered, by the surrounding disk and envelope. As described in Bjorkman & Wood (2001), the radiative equilibrium algorithm corrects for the temperature in each grid cell by sampling the new photon frequency from a differenced emissivity function (the difference between that computed with the previous erroneous temperature and that computed from the new corrected temperature). Energy is conserved and no iteration is required as the difference spectrum corrects for the previous temperature errors. The scattering phase function is approximated using the Henyey-Greenstein function, with forward-scattering parameter, g, and albedo, ω computed at each wavelength from our grain model (described below). Polarization is calculated assuming a Rayleigh-like phase function for the linear polarization (White 1979).

The Monte Carlo codes produce results simultaneously at all inclinations. We also incorporate the "peeling-off" algorithm (Yusef-Zadeh, Morris, & White 1984, Wood & Reynolds 1999) to produce high S/N images at a specific inclination in a given run. Images are produced at several wavelengths and convolved with broadband filter functions for comparison to observations. For this paper, we chose for the near-IR images the Hubble Space Telescope NIC2 F110W (1.1 μm), F160W (1.6 μm), and F205W (2.1 μm) filters. For the mid-IR images, we chose the SIRTF IRAC filter functions at 3.6, 4.5, 5.8, and 8.0 μm. And for the far-IR images, we chose the SIRTF MIPS filter functions at 24, 70, 160 μm. A given run produces all the images simultaneously as it produces the SEDs and polarization spectra. The models take $\sim$ 30 minutes to produce high quality spectra (that is, high frequency resolution and low noise) at all inclinations on a 1 GHz linux PC running g77 FORTRAN. To produce high quality images takes several hours.

2.3. *Dust Model*

The dominant opacity source in the radiative transfer models is dust grains. Our dust model is based on that derived by Kim, Martin, and Hendry (1994) for the diffuse ISM (using a code kindly supplied by Peter Martin and Paul Hendry). To approximate dust properties in nearby star formation regions, we produce a size distribution of grains that fits an extinction curve generated by the Cardelli, Clayton, & Mathis (1989) prescription, with R_V=4. This value of R_V is typical of the denser regions in the Taurus molecular cloud (Whittet et al. 2001). The size distribution is not a simple power law, because it is derived from a Maximum Entropy Method solution. The size distribution is similar to that shown in Figure 1a of Kim et al. (1994). We adopt the dielectric functions of astronomical silicate and graphite from Laor & Draine (1993). To illustrate the effects of ices, which cause observable spectral features, we include a layer of water ice on the grains, covering the outer 5% of radius. We varied this value between 0 and 15% and found 5% to agree best with polarization observations, as discussed in §3.5. The ice dielectric function is taken from Warren (1984).

This grain model may be appropriate for the envelope properties but is likely not applicable in the midplane of the disk where grains should grow to meter-size within a timescale of $10^4 - 10^5$ years (Weidenschilling & Cuzzi 1993; Wetherill & Stewart 1993; Beckwith, Henning, & Nakagawa 2000). Thus, at very long wavelengths where thermal emission from the disk dominates, our SEDs may not agree with observations (see D'Alessio, Calvet, & Hartmann 2001, Wood et al. 2002a for models of disks using large grains). A plot of the grain properties vs. wavelength is shown in Figure 1. The properties for ISM grains are also shown for comparison. The major difference is that the albedo of the R_V=4 grains is substantially higher out to about 10 μm, which will give brighter images at these wavelengths than ISM grains.

3. FOUR VARIATIONS ON A CLASS I SOURCE GEOMETRY

To illustrate the effects of geometry on the SED we will show results for four geometries. The first is the rotationally-flattened infalling envelope only, illuminated by the central star. This is the geometry used by several previous authors (though spherically averaged in some cases). For model parameters, we use typical values derived from previous models of Taurus sources (Kenyon et al. 1993a,b): infall rate, $\dot{M} = 5 \times 10^{-6} M_{\odot}/yr$, centrifugal radius R_c = 100 AU, envelope outer radius R_{max} = 5000

AU, and envelope inner radius equal to the dust destruction radius, about 7.5 stellar radii in this case. The central star radiates as a 4000 K star, using a Kurucz model atmosphere (Kurucz 1994), with a radius of $R_\star = 2.09 R_\odot$, giving a stellar luminosity of 1 $L_\odot$. An azimuthal cut through the envelope density structure is shown in the top-left panel of Figure 2. It has a toroidal shape in the midplane about twice the size of the centrifugal radius. The density profile within this region falls roughly as $\rho \propto r^{-1/2}$ (see equation 1), and beyond this changes to $\rho \propto r^{-3/2}$.

For our second geometry, we add the density structure of the flared disk (equation 3), as shown in the top-right panels of Figure 2b and 2c. This disk has a mass of 0.01 $M_\odot$ and an outer radius equal to the envelope centrifugal radius, 100 AU. For our disk parameters, the dust destruction radius is $7.5R_\star$ which we set as our inner disk radius. For a disk with $\alpha_{disk} = 0.01$, and the disk parameters in Table 1, the fraction of luminosity emitted within the disk (i.e., beyond $7.5R_\star$) is $L_{acc} = 0.0078 L_\star$. The third geometry includes the disk and a streamline cavity with an opening angle, θ_C, of 25°at 5000 AU. And the fourth geometry includes the envelope, disk, and a curved cavity with an opening angle of 20°at 5000 AU. Notice Figure 2b shows that the curved cavity carves out more of the inner envelope material, even though its opening angle at 5000 AU is smaller than the streamline cavity. Table 1 summarizes all the model parameters and Table 2 shows the variations for the four models.

Figure 3 shows a plot of optical extinction vs. polar angle through the envelope to give an idea of the optical depths involved. In Model 1, the rotationally-flattened envelope, the extinction ranges from $A_V = 32$ pole-on to $A_V \sim 225$ at an inclination of 89.999 degrees (the solution for density has a singularity in the midplane). In the models with bipolar cavities (models 3 and 4), the extinction drops to $A_V = 1.5$ near pole-on inclinations. In the models with disks, the extinctions increase to several million at edge-on inclinations. Thus, the star and inner disk radiation will be extincted out to very long wavelengths for the edge-on viewing angles in these models. This radiation can escape through scattering at wavelengths where the albedo is not negligible. Wood et al. (2002a) shows the varying contributions of direct, scattered, and thermal emission for disk models.

3.1. *Temperatures*

Figure 4 shows temperatures calculated from the radiative equilibrium solution in the four geometries. Some interesting features to note are: 1) The low-density bipolar cavities (models 3 and 4) are hotter than the surrounding envelope, since they are exposed to more direct stellar radiation. 4) The midplane is cooler than the envelope or cavity, especially in the models with a disk (Models 2-4) (Figure 4b, 4c). Regions in the midplane beyond about 1 AU see less of the radiation from the star and warm inner regions due to the large optical depths through the disk (Figure 3), and thus are heated less than the surrounding envelope. 4) The interior of the disk in Model 2 is warmer than those in Models 3 and 4 (Figure 4c). This model has no bipolar cavity and thus more radiation is trapped within the envelope to heat the disk.

Figure 5 shows the temperature behavior in different regions in more detail. This plots temperature as a function of radius for four polar angles, $\theta = 0°, 30°, 60°$, and 90°. In Model 1, which has no disk or cavity, the temperature profiles are similar at all inclinations. The equatorial profile is slightly steeper due to the higher optical depths ($A_V = 225$, compared to 33 at the poles). The temperature scales roughly as $r^{-0.5}$ out to about 3 AU, and then transitions to $r^{-0.33}$ beyond 200 AU. As shown in Kenyon et al. (1993a), the temperature profile in optically thin regions is $T \propto r^{-a}$, where $a = -2/(4+p)$, and p is the power law exponent for the grain opacity, i.e., $\kappa_\nu \propto \nu^p$. Beyond a radius of 100 AU, the emitting temperatures are below 40 K, so the peak of the blackbody function is longward of 75 μm. At these wavelengths, the opacity power law exponent is $p = 2$, giving an optically thin temperature profile of $r^{-1/3}$ in agreement with our results. The light grey line plotted with each model is a power law with $a = 0.33$. In the inner region, we can attempt to compare to the diffusion solution, though our opacity exponent varies with wavelength and therefore temperature. The diffusion solution (Kenyon et al. 1993a) gives $T \propto r^{-a}$, where $a = (1+n)/(4+p)$, and n is the density power law exponent, $\rho \propto r^{-n}$. At 1 AU, for the rotational infall solution, $n = 1/2$. The temperature is 400 K, giving peak Planck emission at 7.5 μm. At this wavelength there is a kink in the opacity law, where p varies between 0.5 (on average) to the long wavelength and 1.5 to the short wave. This gives a range of $a = 0.42 - 0.6$ for the calculated temperature profile. Our value of $a = 0.5$ is within this range. Kenyon et al. (1993a) find a value of $a \sim 0.7$ in similar envelope geometries as our Model 1; however, the profiles in Efstathiou & Rowan-Robinson (1991) appear to be closer to $a \sim 0.5$. These differences could be due in part to different grain models and envelope parameters.

The temperature profiles for models with disks and cavities have much more variation with polar angle, as shown in Models 2-4 in Figure 5. The midplane temperature profile shows a steep drop in the disk, with $T \propto r^{-1.15}$ out to 1 AU, and flattening out to 100 AU. Then it follows a similar profile as the rest of the envelope, scaled to a lower temperature. The temperature profile in the polar region in the models with cavities (Models 3-4) is similar to the models without cavities. It flattens out to the optically thin profile, $a = 1/3$, at a smaller radius, leading to higher overall temperatures in the cavity. The 30°and 60°profiles (dotted and dashed lines) diverge from the 0° line where the path intersects the cavity wall, and drops to the lower envelope scale. This happens earlier in Model 3 than Model 4 due to the shape of the cavity walls. At large radii, the models with cavities are hotter along all directions, even in the midplane.

To better understand the temperature behavior in the disk, in Figure 6 we compare the midplane temperature profile of the models with disks (Models 2-4) with those of disks with no envelopes. The grey line plotted with each model is a power law, $T = 90\,(r/1\mathrm{AU})^{-0.4}$ K. It is clear from these plots that no single power law characterizes the temperature behavior in either the disk-only or disk+envelope models. In all of the models except Model 2, the temperatures are similar between about 2-10 AU. In this region, the accretion luminosity is not as important, with the disk temperature determined mostly from stellar flux heating the flared surface. The midplane temperature is higher in Model 2 than any of the others due to extra heating from the surrounding envelope (see also D'Alessio, Calvet, & Hartmann 1997). For Models 3 and 4, the cavities are not providing much additional heating to the disk. As we will show in the next section, the emissivity in the cavities is actually higher than in the same region of the envelope in Model 2. However, this radiation is also able to escape through the cavity in Models 3 and 4, whereas the envelope radiation in Model 2 is trapped and heats up the disk. Beyond about 10 AU, Models 3 and 4 diverge from the disk-only models due to extra heating from the surrounding envelope. In this region, Model 3 is even higher than Model 2, probably due to heating of the cavity walls by stellar radiation (due to their higher curvature, they intercept more stellar radiation).

Inside 1-2 AU, the temperature profiles are the same for all the models with disk accretion, with a power law exponent $a = 1.15$. This is higher than expected for passive accretion ($a = 0.75$; Kenyon & Hartmann 1987), but is in agreement with the plotted profiles of D'Alessio et al. (1998) between 0.1 and 2 AU. The temperature is determined by the accretion luminosity which has a steep falloff with radius (equation 4). Between 0.073 and 0.16 AU (7.51 to 16.4 $R_\star$), the accretion luminosity raises the disk temperature above the dust sublimation temperature of 1600 K. We set the opacity to 0 in this region since the gas opacity is much lower than dust. With surface density of 1300-1400 $\mathrm{g\,cm^{-2}}$ and gas Rosseland mean opacity $\kappa_R \sim 10^{-4}\,\mathrm{cm^2\,g^{-1}}$ (Alexander, Johnson, & Rypma 1983), the vertical gas optical depth through the disk (top and bottom) is $\tau = \Sigma\kappa \sim 0.1$ which is reasonably optically thin (Lada & Adams 1992). For the disk without accretion, the temperature profile exponent is $a = 0.6$ from 0.1-1 AU, then flattens out to $a = 0.4$, and even lower beyond 10 AU. This is in reasonable agreement with blackbody emission models that give $a = 0.5$ for our flared disk with $\beta = 5/4$ (Kenyon & Hartman 1987).

3.2. *Emissivity and Infrared Images*

Even though Figures 4 and 5 show that temperatures in the bipolar cavities are higher than in the envelope, we might expect the overall emitted energy from the cavities to be small due to the low densities. However Figure 7 shows that the high temperatures lead to large emissivities in the cavity, despite the lower densities. This is especially apparent at the longer wavelengths, 24 and 160 μm, shown here. The emissivity is defined as $j_\nu = \kappa_\nu \rho B_\nu$. Figure 7 plots azimuthal slices of the emissivity. It shows how much energy per unit volume is emitted throughout the envelope (but is not a radiative transfer calculation showing how light is propagated through the envelope). Even though the models with bipolar cavities have slightly lower mass than the others, their total emissivities are larger due to the higher temperatures in the cavities. Note that the images are plotted to different size scales for the three wavelengths. Though the magnitude of the emissivity is much lower at longer wavelengths, the brightness profile is much shallower.

Figure 8 shows images that result from the radiation transfer calculations. These are shown at an inclination of $i = 80°$. From top to bottom, the four model geometries are plotted, and from left to right, 3-color composities of near-IR (left), mid-IR (middle), and FIR (right) are plotted. The images are displayed to mimimum flux levels described in the figure caption, assuming a distance to the source of 140 pc. The near-IR images are similar to observations and previous models (Padgett et al. 1999, Stark et al. 2002). The mid-IR images should be detectable by the upcoming Space Infarared Telescope Facility (SIRTF) in nearby star forming regions, and the FIR images should be detectable by SIRTF out to much larger distances. As Figure 7 showed, the mid-IR *thermal* emission should be rather localized near the central source. The large extent of the mid-IR images in Figure 6 results from *scattered* light. As discussed in Figure 1, the albedo of the $R_V = 4$ grains used here is higher than ISM dust at these wavelengths. Since the albedo of the dust is sensitive to grain size, the mid-IR images should be a useful diagnostic of grain size. The FIR images delineate cavity walls and show shadowing in the disk. However, these effects will be completely washed out at SIRTF resolution, which, at 70 μm, has a full width at half maximum (FWHM) of 38″or 2380 AU at a distance of 140 pc. We convolved the images with Gaussian point spread functions broadened to the HST and SIRTF resolution for each wavelength. We don't show them here because the near-IR and mid-IR images are essentially unchanged at the resolution shown here, and the FIR images are washed out and indistinguishable from each other, though they are elongated with about a 2/1 ratio.

3.3. *Spectral Energy Distributions*

The model SEDs are shown in Figure 9. Ten inclinations are plotted, the top curve corresponding to pole-on and the bottom to edge-on. The absorption feature at 3.1 μm is due to ice opacity, and that at 10 μm is due to silicate. A distinctive feature of the SED plots is the broad dip at 10 μm at low inclinations in models that include the flared disk. This is due to the disk geometry and the grain properties: At shorter wavelengths, even though the opacity through the disk and envelope is larger (Figure 3), the albedo increases allowing light to scatter out at all inclinations. Note that the near-IR colors are determined completely by scattering for inclinations $i > 60$ ($\cos i < 0.5$), so the concept of "de-reddening" based on the colors is meaningless since that only applies to direct extincted light, not scattered (see Stark et al. 2002). At wavelengths longward of 10 μm, the opacity decreases enough to allow thermal emission to propagate through the disk and envelope. Near 10 μm, the low albedo and high opacity combine to prevent radiation from escaping at high inclinations.

Another striking feature of the SEDs in Figure 9 is that the models with bipolar cavities (Models 3 and 4) are much brighter at optical/near-IR wavelengths in better agreement with observations than the models without cavities (Kenyon et al. 1993a,b). Notice in Models 3 and 4 that the pole-on inclinations still suffer extinction at short wavelengths due to the dust in the cavity. The shortwave clearly is very sensitive to the amount of dust in the cavity. Models 3 and 4 also show the 10μm silicate feature in emission at pole-on inclinations, due to low optical depth to the source of emission (the inner disk surface).

It is clear from the plots in Figure 9 that the more edge-on spectra have lower integrated fluxes than other inclinations. In a spherical source, the integral of the measured SED multiplied by $4\pi d^2$, where d is the distance to the source, is equal to the luminosity of the source. However, this is not true for sources with non-spherical envelopes, where the SED must be integrated over direction as well as frequency, i.e.,

$$L = 2\pi d^2 \int_{\mu=-1}^{1} \int_{\nu=0}^{\infty} F_\nu d\nu d\mu, \tag{7}$$

where $\mu = \cos i$ and i is the inclination, also the polar angle. We note that in our models, this integral is equal to our input luminosity to within 0.02% (the difference is due to performing the integral after coarsely binning the results in angle, since flux is fully conserved in our models). Figure 10 shows the correction factor that would have to be applied to the integrated SED at a single inclination to get the true luminosity of the source. The correction factor is simply the luminosity divided by the integrated SED at each inclination i,

$$\text{correction} = \frac{\frac{1}{2}\int_{-1}^{+1}\int_\nu F_\nu d\nu d\mu}{\int_\nu F_\nu(i) d\nu}. \tag{8}$$

As Figure 10 shows, the observed SEDs can estimate the luminosity of a source only to within a factor of 2. While it is not surprising that the edge-on integrated flux is lower than the true luminosity, it is interesting to note that the pole-on integrated flux is a factor of 2 larger than the true luminosity for the sources with bipolar cavities. This inclination receives a maximum of direct stellar flux, scattered flux and reprocessed emission.

Nakazato et al. (2003) defined a parameter, f_L, as the ratio of the integrated SED, $\int F_\nu d\nu$ to the peak flux νF_ν, and argued that this can be used as an indicator of inclination. We had to modify their definition slightly because for our models with cavities, the wavelength of the peak shifts from about 70 μm to 1.6 μm at the pole-on inclinations, causing f_L to decrease for pole-on inclinations. We can resolve this by defining $f_L(FIR)$ to be the ratio of the SED to the peak flux in the far infrared (FIR). Figure 11 plots $f_L(FIR)$ vs. inclination for our set of models. Our models also show a correlation with inclination, but the behavior is different from Nakazato et al.'s values. This is due to the differences in our model geometries. Nakazato et al. include an envelope, disk and cavity in their models but their envelope is spherically symmetric up to the cavity opening angle. Thus, their f_L is relatively flat up to the cavity opening angle and then flat within the cavity at a high value. In contrast, our models using a rotationally flattened envelope show a more gradual increase in $f_L(FIR)$ as the inclination becomes more pole-on (increasing $\cos i$), due to varying envelope extinction with polar angle, a different cavity shape, and a different assumption for the dust content in the cavity. Thus, the behavior of f_L with inclination depends strongly on model assumptions. Nakazato et al. claim this parameter f_L can determine inclination to $\pm 5°$, and use as an example IRAS 04365+2535 for which they find an inclination of 20°. However, the high near-IR polarization ($P_K \sim 10-15\%$; Whitney et al. 1997, Lucas & Roche 1998), and molecular outflow observations (Chandler et al. 1996) suggest inclinations of $i \sim 40° - 70°$. We suggest that more detailed modeling, including as much observational information as possible, is required to "calibrate" the models before applying this factor based on SED information alone.

3.4. *Color-Color Plots*

Figure 12 shows color-color plots for our models. The black crosses are main sequence/giant branch stars, and the dotted lines extending from them show the reddening lines. The region enclosed by these lines shows where the MS/GB falls on these plots. The model points are plotted with different shades of grey representing inclination, with light grey representing pole-on, and black edge-on. The models without cavities are shown by the filled circles (Model 1) and asterisks (Model 2). The models with cavities are shown by open triangles (Model 3) and open diamonds (Model 4). The models with cavities are substantially bluer in all the plots. In a source observed to have a bipolar cavity (as indicated by images resembling Figure 8, outflows, and high polarization), it is clear from Figure 12 that 2-D cavity models should be used to interpret their colors. Using 1-D models, or models without bipolar cavities, would lead to assignment of a later evolutionary state to the source than is appropriate. Another interesting feature in Figure 12 is that some of the edge-on sources are the bluest. This is because the disk blocks all the direct light, leaving only scattered light which is blue, especially in the MIR where the albedo increases steeply towards shorter wavelengths.

The bottom left panel of Figure 12 shows that the Class I source colors are well-separated from reddened main sequence and red giant stars for this particular color choice in the mid-IR and our grain model. The bottom right panel, plotting [3.6]-[5.8] vs [8.0]-[24.0] shows that Class I sources are very red for this color choice. The main sequence stars have to be reddened by at least $A_V \gtrsim 100$ to overlap with these sources. Thus, in nearby star forming clouds, where foreground main sequence stars have almost no reddening, the Class I sources will likely stand out. Our next paper will explore in more detail how well different evolutionary states are separated in color-color space.

3.5. *Polarization*

An additional tool to distinguish the various geometries as well as grain properties is the polarization spectrum, shown in Figure 13. Plotted is $Q = P\cos(\chi)$, where χ is the orientation of the polarization vector. Because these models are axisymmetric, and the grains are spherical (no dichroism), the integrated or net polarization is either parallel or perpendicular to the rotation axis. If Q/I is less than 0, the net polarization is perpendicular to the rotation axis. This is the case over much of the spectrum because most of the scattered light emerges from the bipolar cavity regions. In all of the models, the polarization is highest for the edge-on inclinations and decreases to 0 pole-on. The polarization is sensitive to the envelope optical depth: To get high polarization from scattered light requires optical depths to the unpolarized stellar/disk radiation of $\tau > 5$ (Whitney et al. 1997). We see this transition in the 1-10 μm region, depending on inclination. At longer wavelengths, more scattered radiation emerges from the equatorial region because the optical depths in the polar regions are too low. We should expect to see the polarization reverse sign at these wavelengths. However, the grain albedo is decreasing rapidly in this region so the polarization vanishes before reversing sign (though there is a hint in Model 4 of a polarization reversal). In a less embedded source we would expect the polarization to reverse sign at a shorter wavelength so the polarization reversal would occur before the albedo drops to 0. We will explore this in more detail in future papers. In disks, where the grains are larger, the albedo should remain higher towards longer wavelengths (Wood et al. 2002a). Thus, polarization spectra should be a useful diagnostic of grain growth as well as evolutionary state.

Figure 13 also shows the behavior of polarization across the ice band feature at 3 μm. The polarization increases across these features because the opacity increases. With higher opacity, less direct (unpolarized) light is present to dilute the polarized light. This behavior agrees with observations across the 3μm feature (Hough et al. 1996, Kobayashi et al. 1999, Holloway et al. 2002).

4. CONCLUSIONS

We have shown that 2-D models of realistic Class I source geometries produce substantially different SEDs from 1-D and simplified 2-D models. The inclusion of a flared disk and bipolar cavity changes the SEDs and colors substantially. The effect of the disk is to cause a broad dip near 10 μm in nearly edge-on sources ($i > 80°$), and the cavity allows more shortwave radiation to escape at all inclinations. Both the disk and cavity introduce inclination effects much greater than the simple rotational infall model gives (Model 1). In addition to the spectral shape, the integral of the SED also varies with inclination. In 1-D models, this integral is equal to the luminosity of the source. In 2-D or 3-D models, the flux must be integrated over direction as well, as shown in equation (7). This is impossible to do for an observed source which is only viewed from one direction. Figure 10 shows the correction that would have to be applied to a source with the same geometry as our models to get the true luminosity of the source for a given inclination.

Nakazato et al. (2003) claim that the inclination can be determined from a factor f_L which is the ratio of the integral of the SED to the peak of $F_\nu d\nu$. Our models give a different behavior for f_L due to the different envelope geometry. We conclude that f_L on its own is not a robust indicator of inclination. Perhaps incorporating many more observational constraints to the models could provide some calibration to this factor.

We placed our model results on color-color plots (Figure 12) for easier comparison to observations, and find that the models with bipolar cavities are much bluer than those without. In addition, the models with cavities show a large spread with inclination. It is clear from these plots that realistic 2-D models are required to properly interpret the colors of Class I sources with bipolar cavities. A 1-D model would require a lower envelope mass to fit the same colors, which would imply a later evolutionary state for the source than is appropriate.

The images in Figure 8 and polarization spectra in Figure 13 can be used to understand dust properties in star forming regions. Our dust model, fit to the extinction curve typical in the Taurus molecular cloud, has enough scattering albedo in the mid-IR to produce extended scattered-light images in the mid-IR. As shown in Figure 1, this albedo is higher than the ISM value. These images are most easily detected at edge-on inclinations where the flared disk blocks the bright direct stellar and inner-disk radiation. The sensitivity of SIRTF may be enough to image these sources and confirm the higher albedo due to larger grains. The polarization spectra also provide constraints on both envelope geometry and grain properties. Our choice of an ice mantle occupying 5% of the outer radius of the grains gives a 3.1 μm feature in good agreement with observations. Further models at different evolutionary states will be needed to better characterize the polarization behavior in protostars.

Given that bipolar cavities and inclination effects introduce a large spread in observational parameters for Class I sources, we suggest that images, outflows, and polarization measurements can aid in determining cavity geometry and inclination. Then 2-D models can more accurately assign envelope mass and evolutionary states to Class I sources. In our next paper we will explore in more detail the effects of evolution on the SEDs, colors, images, and polarization of protostars.

We thank Martin Cohen for providing the colors of main sequence/giant branch stars in Fig. 12, as well as providing zero-point magnitude scales for several SIRTF wavebands. This work was supported by the National Science Foundation (AST-9909966, AST-9819928) and the NASA Astrophysics Theory Program (NAG5-8587). K. Wood acknowledges support from the UK PPARC Advanced Fellowship.

REFERENCES

Adams, F. C., Lada, C. J., & Shu, F. H. 1987, ApJ, 308, 788
Alexander, D. R., Johnson, H. R., & Rypma, R. L. 1983, ApJ, 272, 773
André, P., Ward-Thompson, D., & Barsony, M. 1993, ApJ, 406, 122
Bachiller, R. & Tafalla, M. 1999, in The Origin of Stars and Planetary Systems, eds. C. J. Lada & N. D. Kylafis (Dordrecht: Kluwer), p. 227
Bate, M. R. 1998, ApJ, 508, 95
Beckwith, S. V. W., Sargent, A. I., Chini, R. S., & Gusten, R. 1990, AJ, 99, 924
Beckwith, S. V. W., Henning, T., & Nakagawa, Y. 2000, in Protostars and Planets IV, eds. V. Mannings, A. P. Boss, S. R. Russell (Tucson: University of Arizona Press), p. 533
Bjorkman, J. E., & Wood, K. 2001, ApJ, 554, 615
Bjorkman, J. E. 1997, in Stellar Atmospheres: Theory and Observations, ed J.P. De Greve, R. Blomme, and H. Hensberge (New York:Springer), 239
Bjorkman, J. E., Whitney, B. A., & Wood, K. 2003, BAAS, 203, 4910.
Burrows, C. J., et al. 1996, ApJ, 473, 437
Cardelli, J. A., Clayton, G. C., & Mathis, J. S. 1989, ApJ, 345, 245
Cassen, P., & Moosman, A. 1981, Icarus, 48, 353
Chandler, C. J., Terebey, S., Barsony, M., Moore, T. J. T., Gautier, T. N. 1996, ApJ, 471, 308
Ciolek, G. E., & Königl, A. 1998, ApJ, 504, 257
Cohen, M., Emerson, J. P., & Beichman, C. A. 1989, ApJ, 339, 455
D'Alessio, P., Calvet, N., & Hartmann, L. 1997, ApJ, 474, 397
D'Alessio, P., Cantó, J., Calvet, N., & Lizano, S. 1998, ApJ, 500, 411
D'Alessio, P., Calvet, N., & Hartmann, L. 2001, ApJ, 553, 321
Dutrey, A., Guilloteau, S., & Simon, M. 1994, å, 286, 149

Efstathiou, A. & Rowan-Robinson, M 1991, MNRAS, 252, 528
Foster, P., & Chevalier, R. A. 1993, ApJ, 416, 303
Galli, D., & Shu, F. H. 1993a, ApJ, 417, 220
Galli, D., & Shu, F. H 1993b, ApJ, 417, 243
Gómez, M., Whitney, B. A., & Kenyon, S. J. 1997, AJ, 114, 265
Hartmann, L. 1998, Accretion Processes in Star Formation (Cambridge: University Press)
Hogerheijde, M. R., van Dishoeck, E. F., Blake, G. A., van Langevelde, H. J. 1998, ApJ, 502, 315
Holloway, R. P., Chrysostomou, A., Aitken, D. K., Hough, J. H., & McCall, A. 2002, MNRAS, 336, 425
Hough, J. H., Chrysostomou, A., Messinger, D. W., Whittet, D. C. B., Aitken, D. K., & Roche, P. F. 1996, ApJ, 461, 902
Ivezìc, Z., Groenewegen, M. A. T., Men'shchikov, A., & Szczerba, R. 1997, MNRAS, 291, 121
Kenyon, S. J. & Hartmann, L. 1987, ApJ, 323, 714
Kenyon, S. J., Calvet, N., & Hartmann, L. 1993a, ApJ, 414, 676
Kenyon, S. J., Whitney, B., Gómez, M., & Hartmann, L. 1993b, ApJ, 414, 773
Kim, S.-H., Martin, P. G., & Hendry, P. D. 1994, ApJ, 422, 164
Kobayashi, N., Nagata, T., Tamura, M., Takeuchi, T., Takami, H., Kobayashi, Y., & Sato, S. 1990, ApJ, 517, 256
Koerner, D. W., & Sargent, A. I. 1995, AJ, 109, 2138
Kurucz, R. L. 1994, CD-ROM 19, Solar Model Abundance Model Atmospheres (Cambridge: SAO)
Lada, C. J. 1987, in Star Forming Regions, edited by M. Peimbert & J. Jugaka, Kluwer, Dordrecht, 1
Lada, C. J. & Adams, F. C. 1992, ApJ, 393, 278
Laor, A. & Draine, B. T. 1993, ApJ, 402, 441
Li, Z.-Y. 1998, ApJ, 497, 850
Lynden-Bell, D. & Pringle, J. E. 1974, MNRAS, 168, 603
Lucas, P. W., & Roche, P. F. 1997, MNRAS, 286, 895
Lucas, P. W., & Roche, P. F. 1998, MNRAS, 299, 699
Moriarty-Schieven, G. H., Wannier, P. G., Tamura, M., & Keene, J. 1992, ApJ, 400, 260
Moriarty-Schieven, G. H., Butner, H. H., & Wannier, P. G. 1995a, ApJ, 445, 55
Moriarty-Schieven, G. H., Wannier, P. G., Mangum, J. G., Tamura, M., & Olmsted, V. K. 1995b, ApJ, 455, 190
Myers, P. C., Fuller, G. A., Mathieu, R. D., Beichman, C. A., Benson, P. J., Schild, R. E., & Emerson, J. P. 1987, ApJ, 319, 34
Nakazato, T., Nakamoto, T., & Umemura, M. 2003, ApJ, 583, 322
Padgett, D. L., Brandner, W., Stapelfeldt, K. R., Strom, S. E., Terebey, S., & Koerner, D. 1999, AJ, 117, 1490
Pringle, J. E. 1981, ARAA, 19, 137
Reipurth, B., & Raga, A. C. 1999, in The Origin of Stars and Planetary Systems, eds. C. J. Lada & N. D. Kylafis (Dordrecht: Kluwer), p. 267
Reipurth, B., Yu, K. C., Heathcote, S., Bally, J., & Rodríguez, L. F. 2000, ApJ, 120, 1449
Saito, M., Kawabe, R., Ishiguro, M., Miyama, S. M., & Hayashi, M. 1995, ApJ, 453, 384
Shakura, N.I., & Sunyaev, R.A. 1973, å, 24, 337
Stark, D. P., Whitney, B. A., Stassun, K., & Wood, K. 2002, in preparation
Strom, K. M., Newton, G., & Strom, S. E. 1989, ApJS, 71, 183
Tamura, M., Ohashi, N., Naomi, H., Itoh, Y., Moriarty-Schieven, G. H. 1996, AJ, 112, 2076
Terebey, S., Shu, F. H., & Cassen, P. 1984, ApJ, 286, 52
Ulrich, R. K. 1976, ApJ, 210, 377
Warren 1984, Appl. Opt., 23, 1206
Weidenschilling, S. J., & Cuzzi, J. N., 1993, in Protostars & Planets III, p. 1031
Wetherill, G. W. & Steward, G. R. 1993, Icarus, 106, 190
White, R. L. 1979, ApJ, 229, 954
Whitney, B. A., & Hartmann, L. 1993, ApJ, 402, 605
Whitney, B. A., Kenyon, S. J., & Gómez, M. 1997, ApJ, 485, 703
Whitney, B. A., & Wolff, M. J. 2002, ApJ, 574, 205
Whittet, D. C. B., Gerakines, P. A., Hough, J. H., & Shenoy, S. S. 2001, ApJ, 547, 872
Wood, K., & Reynolds, R. J. 1999, ApJ, 525, 799
Wood, K., Wolff, M. J., Bjorkman, J. E., & Whitney, B. 2002a, ApJ, 564, 887
Wood, K., Lada, C. J., Bjorkman, J. E., Kenyon, S. J., Whitney, B., & Wolff, M. J. 2002b, ApJ, 567, 1183
Yusef-Zadeh, F., Morris, M., & White, R. L. 1984, ApJ, 278, 186

Table 1
Model Parameters

Parameter	Description	Value
$R_\star$	Stellar radius	2.09 $R_\odot$
$T_\star$	Stellar temperature	4000 K
$L_\star$	Stellar luminosity	1 $L_\odot$
$M_\star$	Stellar mass	0.5 $M_\odot$
$M_{\rm disk}$	Disk mass	0.01 $M_\odot$
α	Disk radial density exponent	2.25
β	Disk scale height exponent	1.25
h_0	Disk scale height at $R_\star$	0.01
$R_{\rm d,min}$	Disk inner radius	7.5 $R_\star$
$R_{\rm d,max}$	Disk outer radius	100 AU
$\alpha_{\rm disk}$	Disk Viscosity parameter	0.01
$L_{\rm acc}(R_{\rm d,min})$	Disk accretion luminosity to $R_{d,min}$	0.0078 $L_\star$
$\dot{M}_{\rm disk}$	Disk accretion rate	$1.4 \times 10^{-8} M_\odot$/yr
$R_{\rm e,min}$	Envelope inner radius	7.5 $R_\star$
$R_{\rm e,max}$	Envelope outer radius	5000 AU
$\dot{M}_{\rm env}$	Envelope infall rate	5×10^{-6} $M_\odot$/yr

Table 2
Model Variations

Name	Disk	Cavity	Cav. shape	θ_C	Env. Mass
Model 1	n	n	...	...	$0.189 M_\odot$
Model 2	y	n	...	...	$0.189 M_\odot$
Model 3	y	y	Streamline	25°	$0.177 M_\odot$
Model 4	y	y	Curved	20°	$0.176 M_\odot$

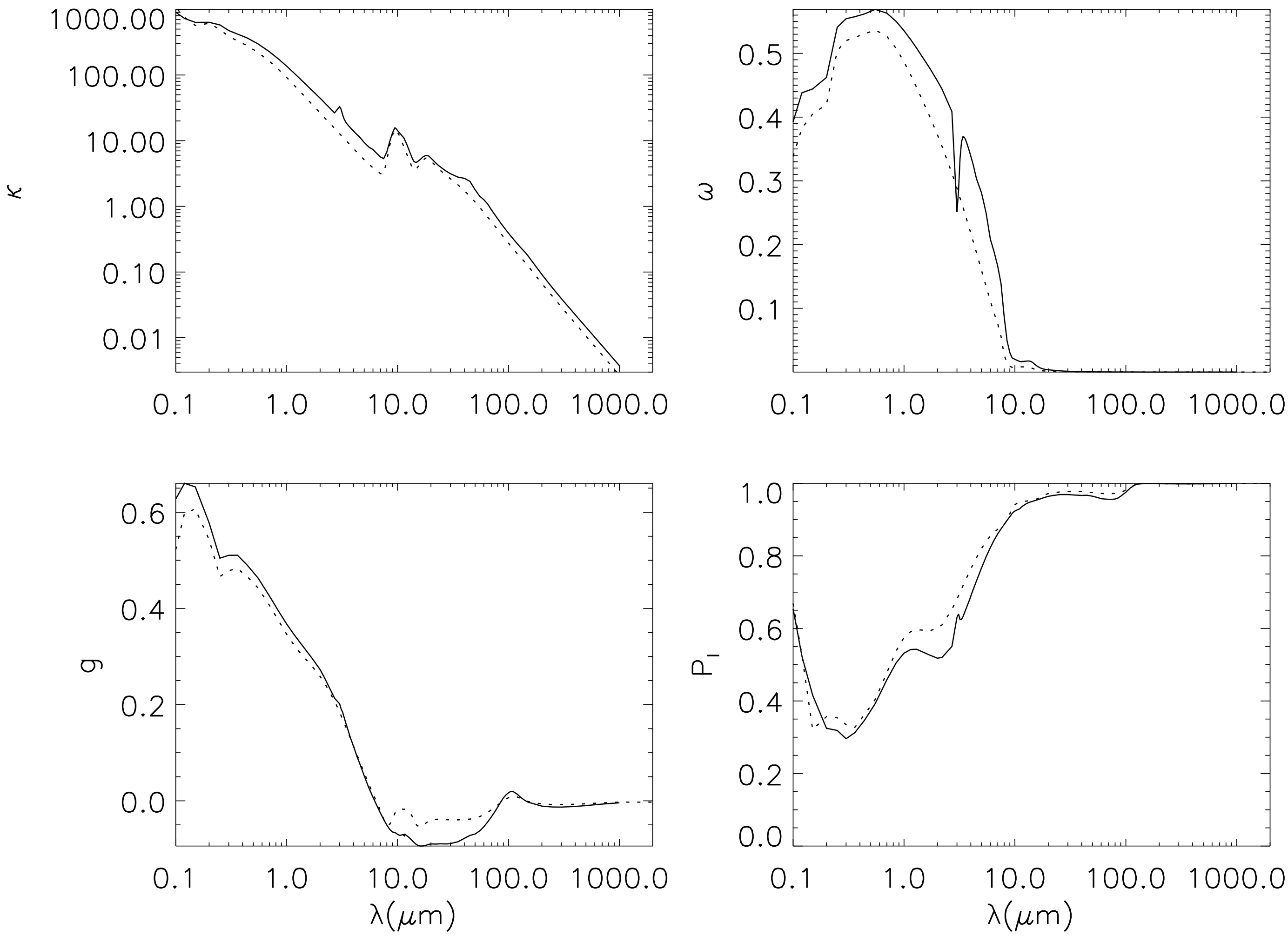

FIG. 1.— Behavior of the $R_V = 4$ grains with wavelength. For comparison, the dotted lines show behavior of ISM grains ($R_V = 3.1$).Top left: opacity, κ; top right: albedo, ω; bottom left: average cosine of scattering angle, g; bottom right: maximum polarization, p_l.

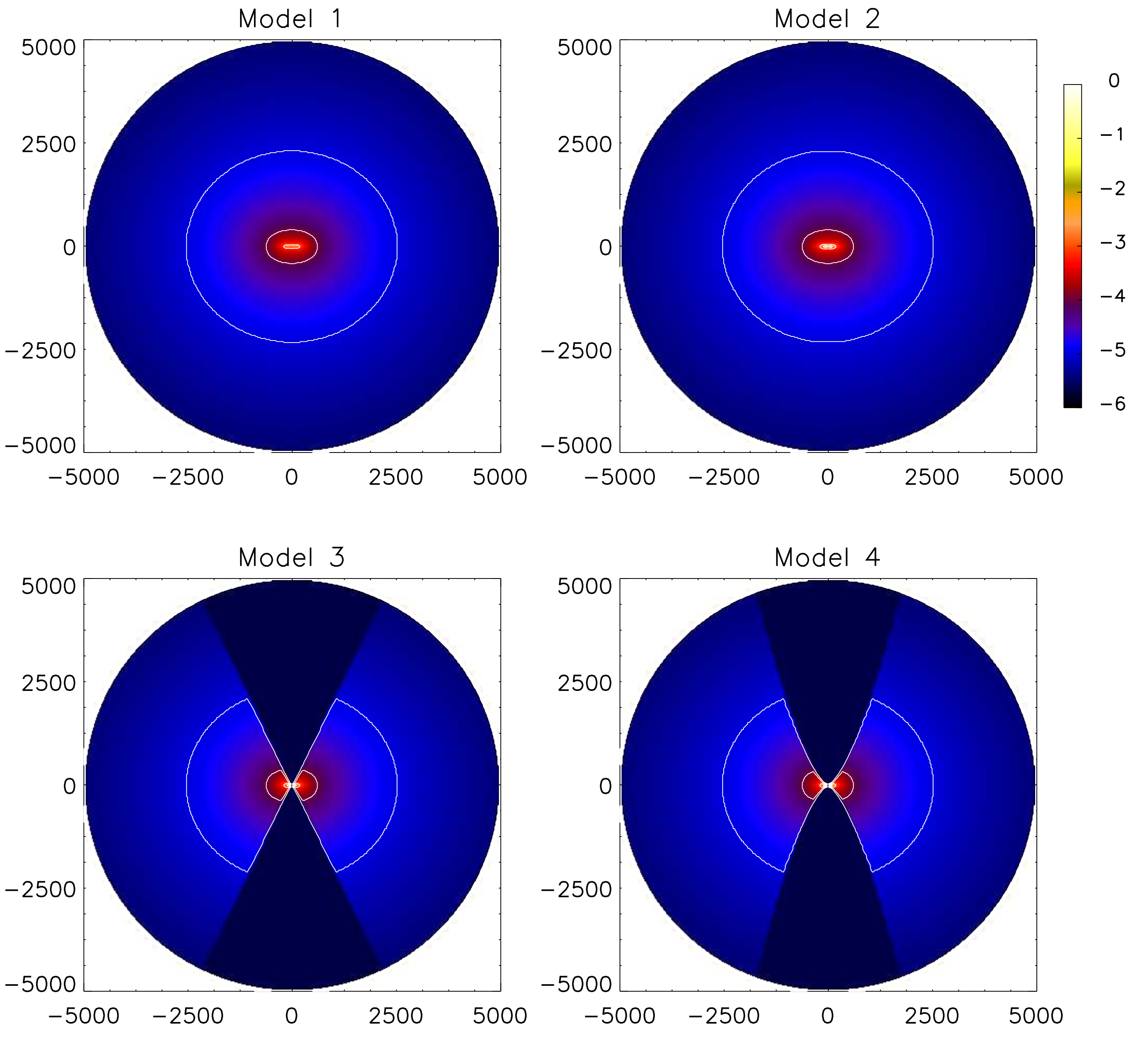

FIG. 2.— Density plots showing the four geometries. Model 1: rotationally flattened infalling envelope; Model 2: same as Model 1 + flared disk; Model 3: same as Model 2 + streamline cavity; Model 4: same as Model 2 + curved cavity. The scaling is logarithmic, plotted to six orders of magnitude from the peak shown. The contours each decrease by 1 order of magnitude, and match the labels of the color bar. The plotted regions and peak densities are (a) 5000 AU, 3×10^{-14}gm cm^{-3}, (b) 300 AU, 1.5×10^{-12}gm cm^{-3}, and (c) 20 AU, 8×10^{-12}gm cm^{-3}.

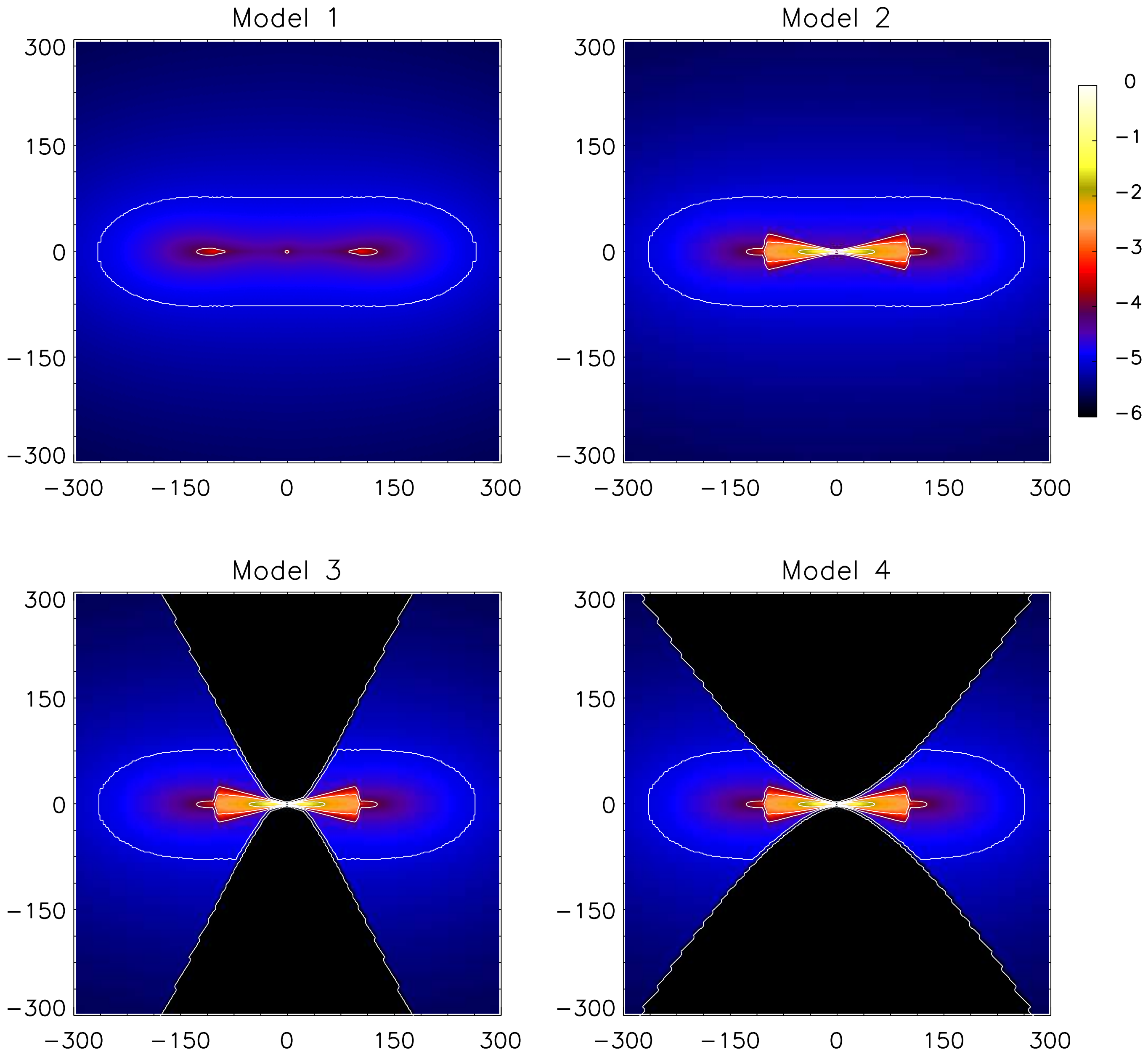
Model 1
Model 2
Model 3
Model 4
300
150
0
−150
−300
−300
−150
0
150
300
0
−1
−2
−3
−4
−5
−6

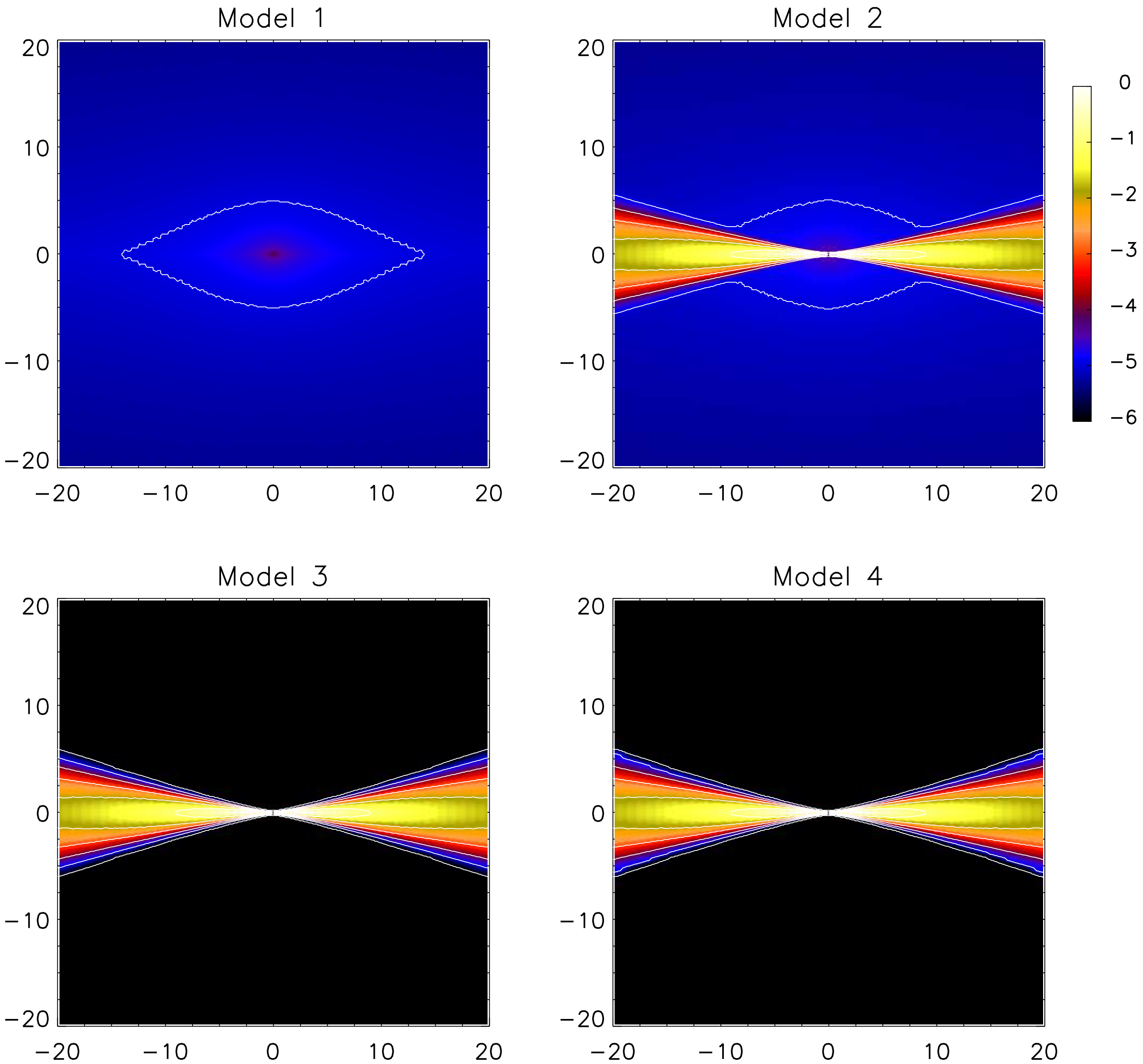
Model 1
Model 2
Model 3
Model 4
20
10
0
−10
−20
−20 −10 0 10 20
0
−1
−2
−3
−4
−5
−6

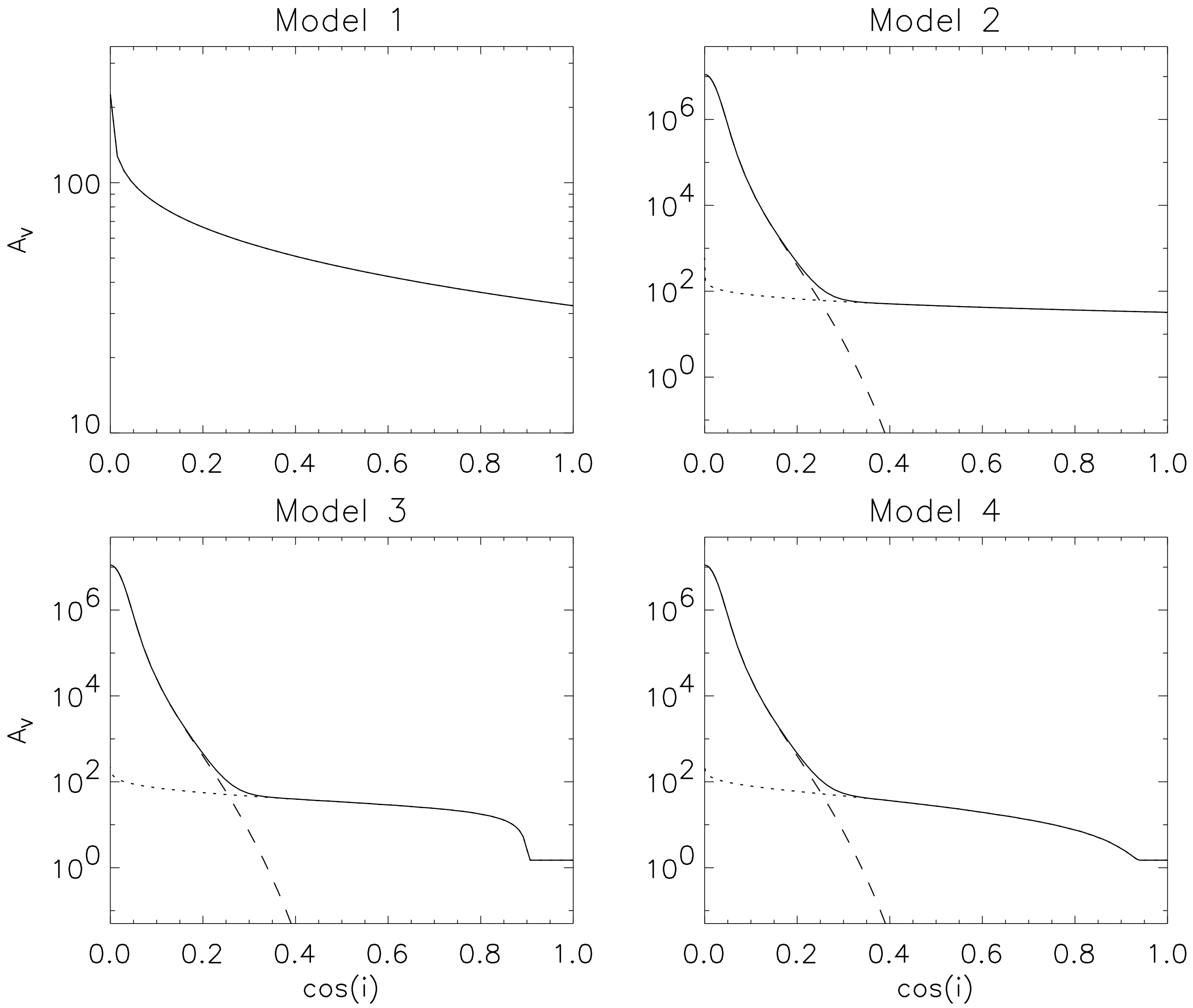

FIG. 3.— Optical extinction, A_V, from the central star through the envelope vs. inclination with respect to the polar axis, i. The dotted line shows extinction due to the envelope, the dashed line is that of the disk, and the solid is the sum. Note the large extinctions at edge-on inclinations for models with disks (Models 2-4).

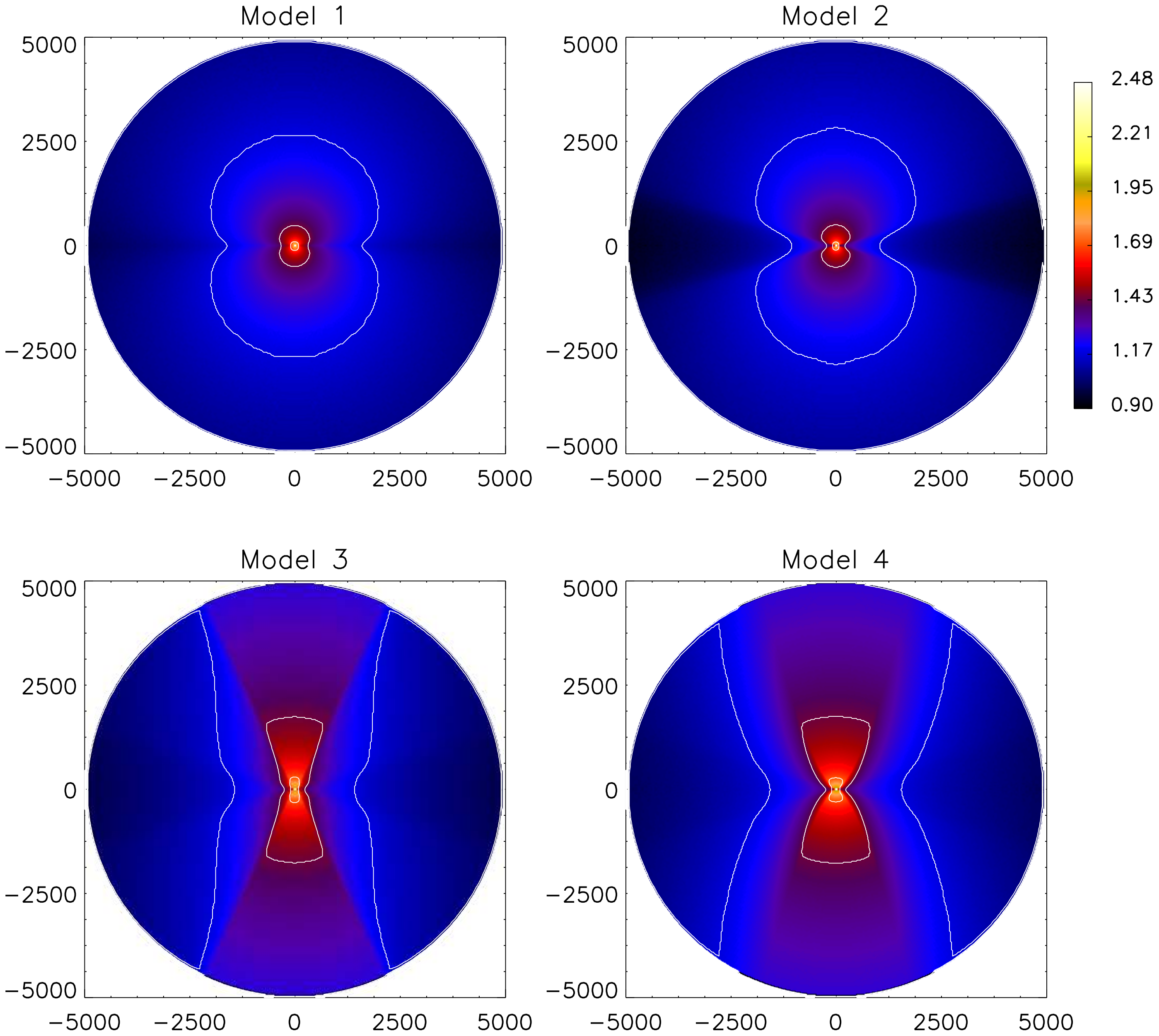

FIG. 4A.— Temperature plots for the 4 geometries. Images are scaled logarithmically with the color scale shown at the right. The contours correspond to the labelled values on the color bar (in units of $log(T)$). The plotted regions and temperature scales are (a) 5000 AU and $T = 8 - 300°$K, (b) 300 AU, $T = 22 - 1000°$K, and (c) 20 AU, $T = 42 - 1600°$K.

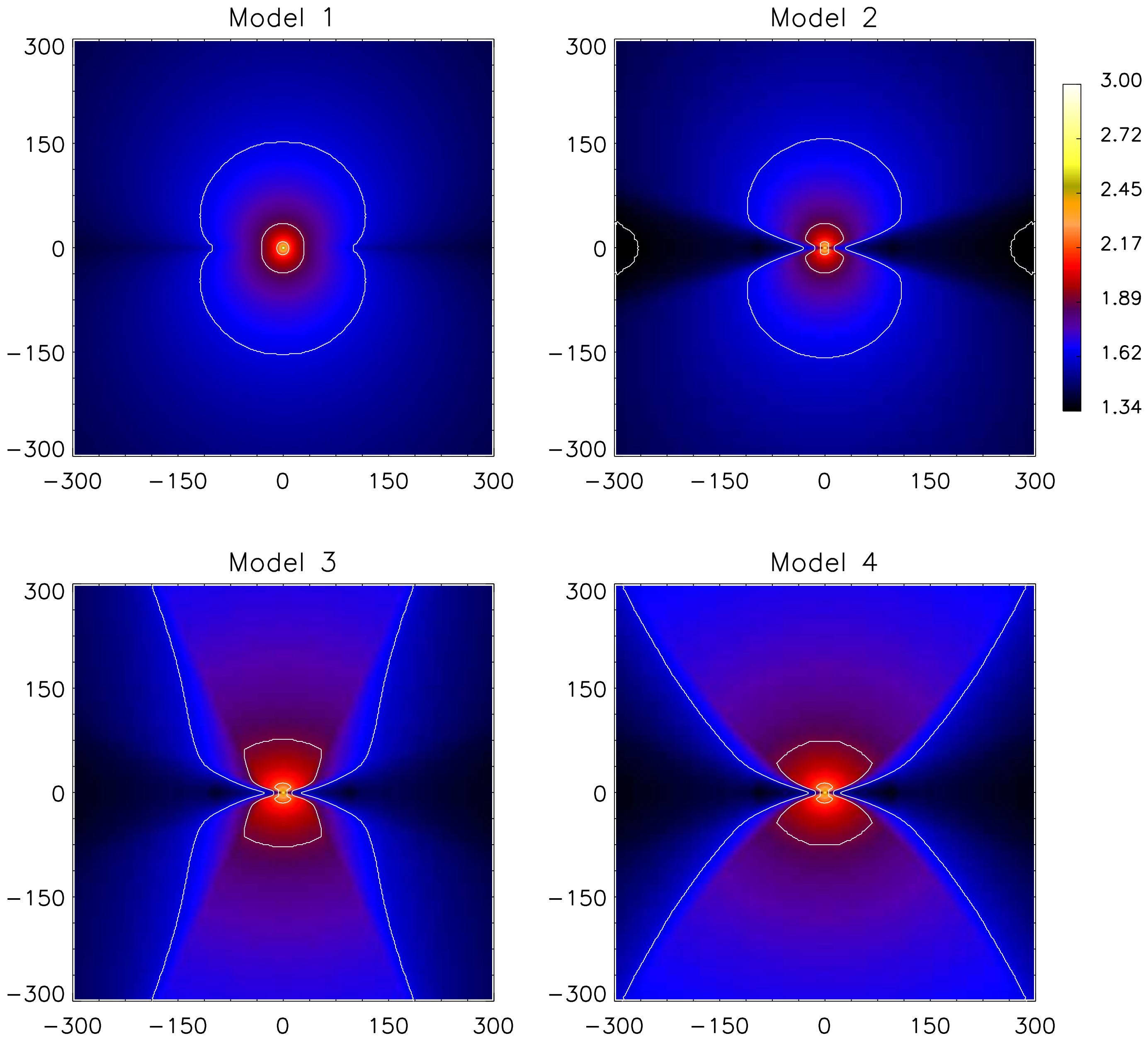
Model 1
Model 2
Model 3
Model 4
300
150
0
−150
−300
−300
−150
0
150
300
3.00
2.72
2.45
2.17
1.89
1.62
1.34

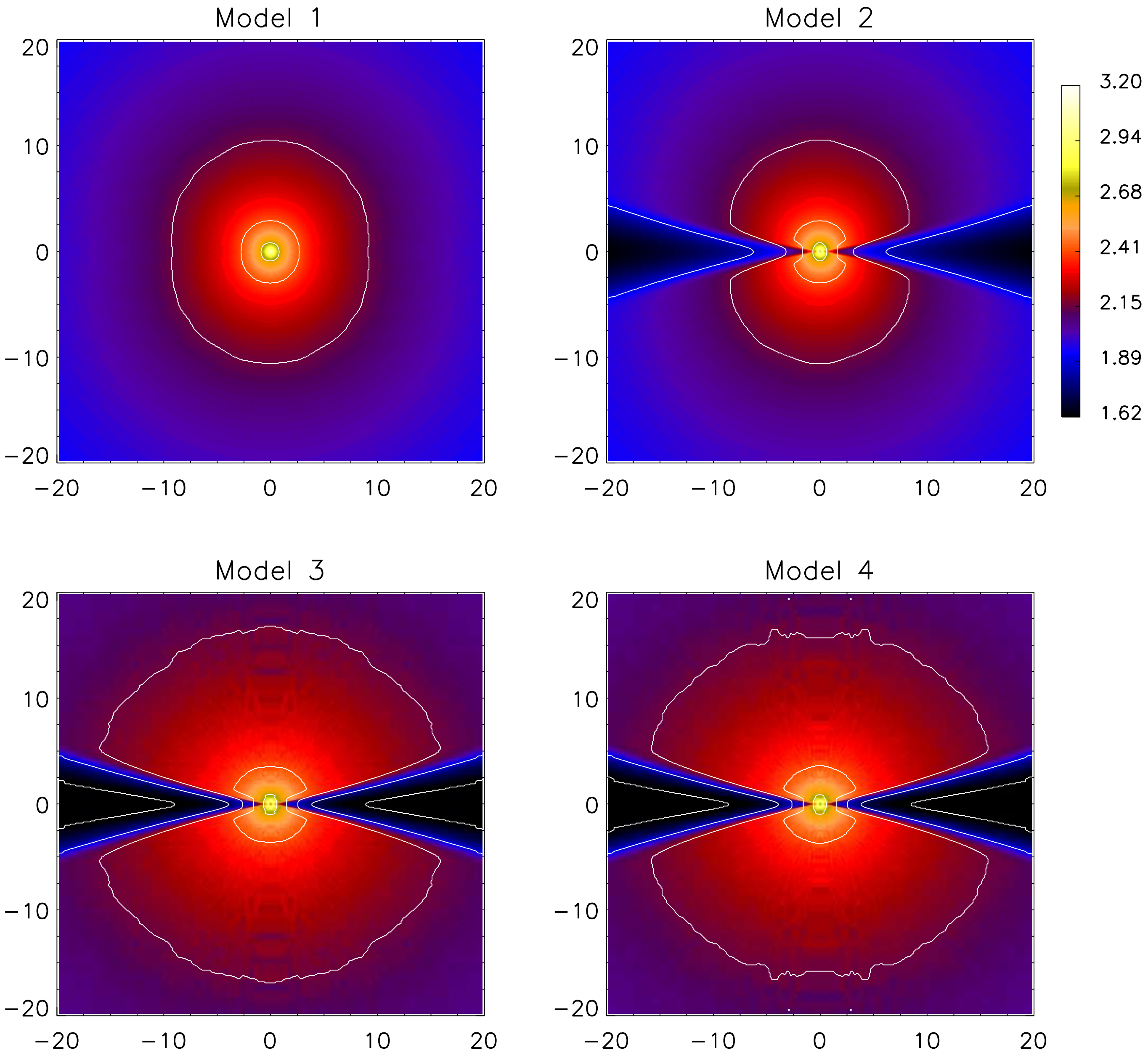
Model 1
Model 2
Model 3
Model 4
3.20
2.94
2.68
2.41
2.15
1.89
1.62

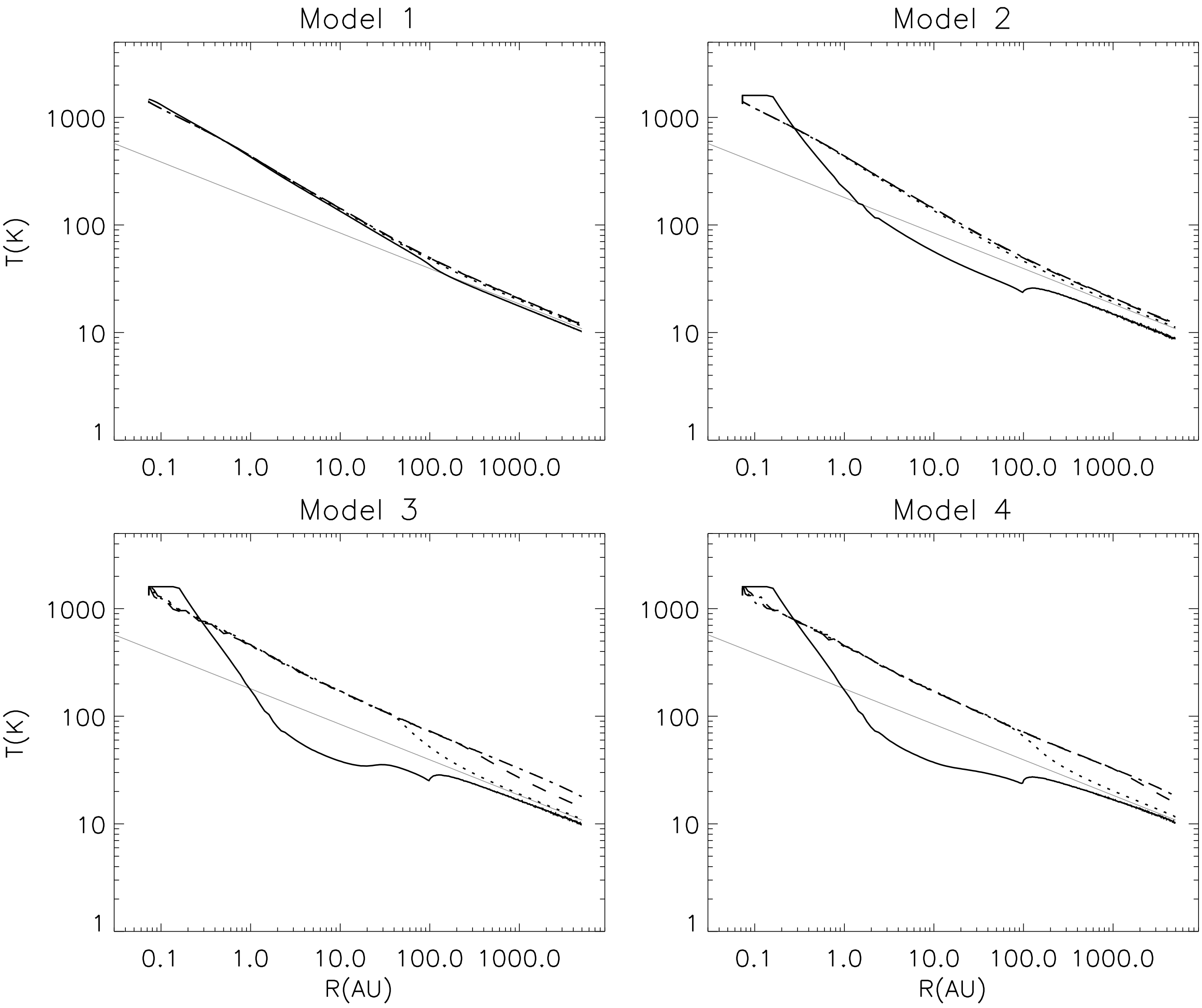

FIG. 5.— Temperature as a function of radius along four co-latitudes, θ, with respect to the polar axis: $\theta = 0$ (dot-dashed line), $\theta = 30$ (dashed), $\theta = 60$ (dotted), and $\theta = 90$ (solid). The light grey line is a power law, $T = 180\,(r/1\mathrm{AU})^{-0.33}$ K

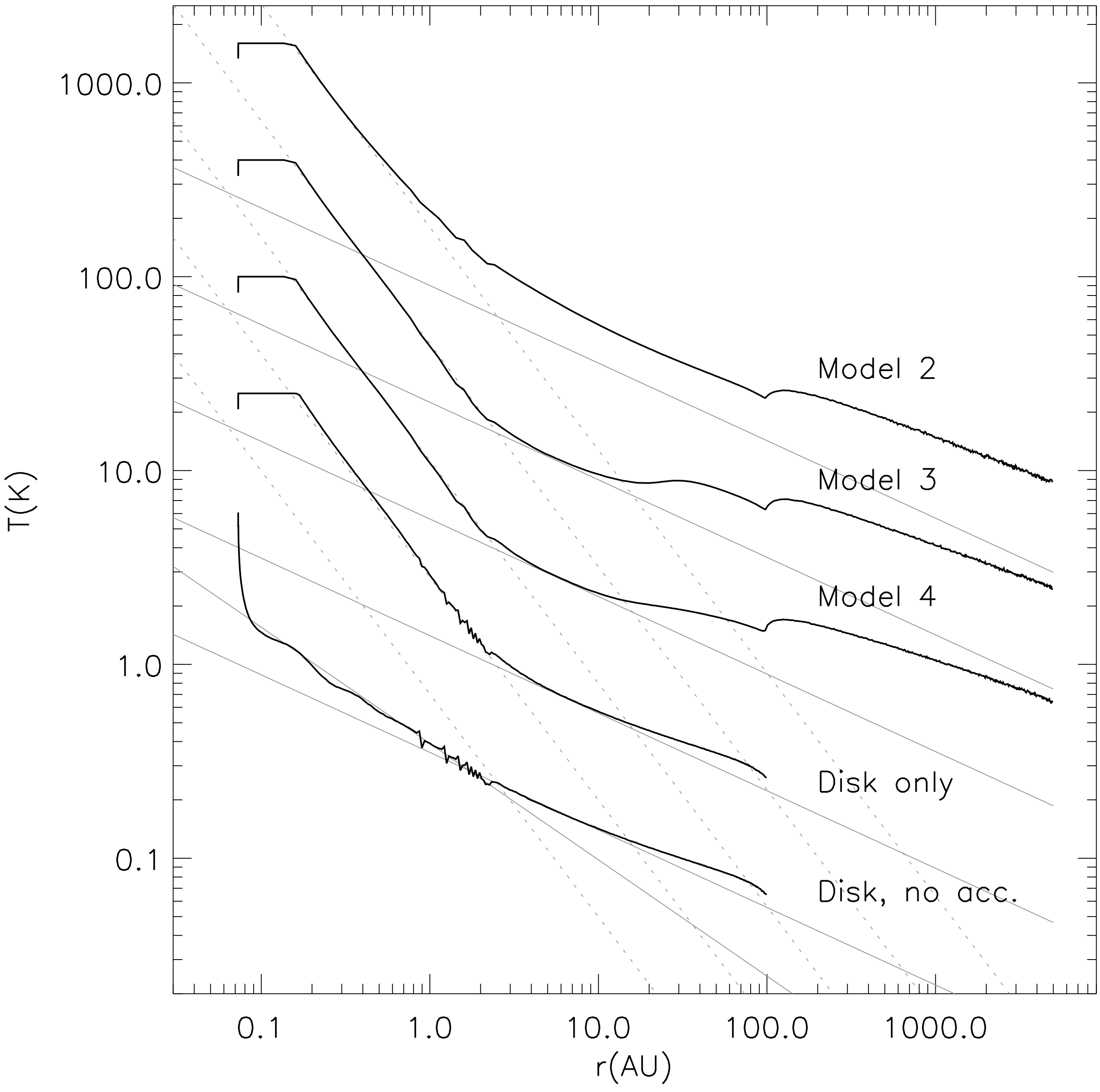

FIG. 6.— Temperature as a function of radius in the midplane of selected models with disks. Each model below the top is scaled down by a factor of four from the one above. The grey line is a power law, $T = 90\,(r/1\mathrm{AU})^{-0.4}$ K, also scaled down by a factor of four for each model. Notice that the disk midplane is warmer throughout the Model 2 disk due to radiation from the surrounding envelope.

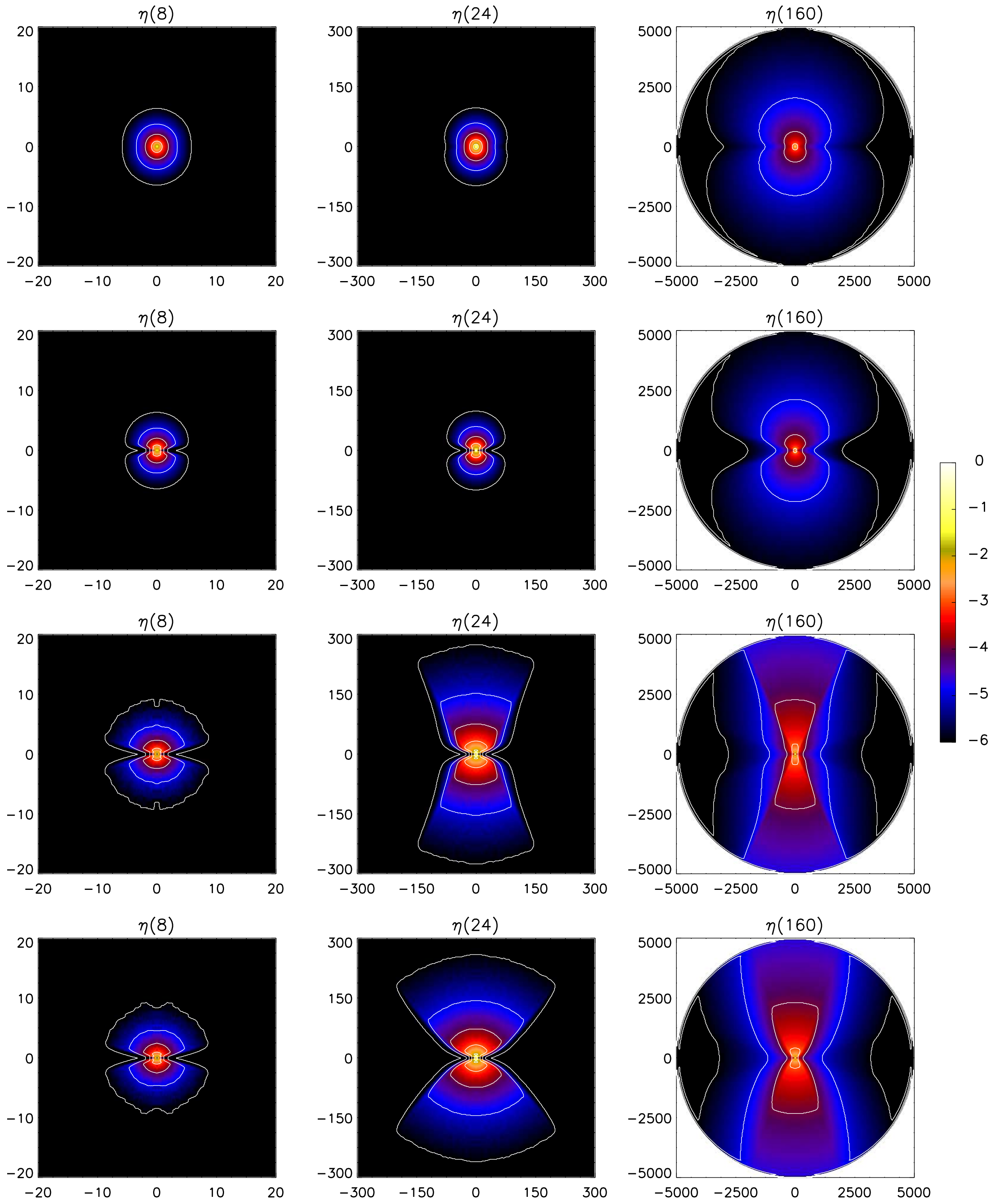

FIG. 7.— Emissivity plots at three wavelengths: 8 μm (left), 24 μm (middle) and 70 μm (right). The four model geometries are plotted from top to bottom. The scaling is logarithmic with the color bar shown on the right, scaled to the peak. Peak emissivities plotted are 1.5×10^{-1} at 8 μm, 1.5×10^{-4} at 24 μm, and 3×10^{-9} at 160 μm, in units of erg/cm^3/s/Hz/sr. From left to right the region plotted spans a radius of 20, 300, and 5000 AU. The emission is more centrally concentrated at shorter wavelengths and in models without cavities (Models 1, 2). The contours each decrease by 1 order of magnitude, starting from the peak.

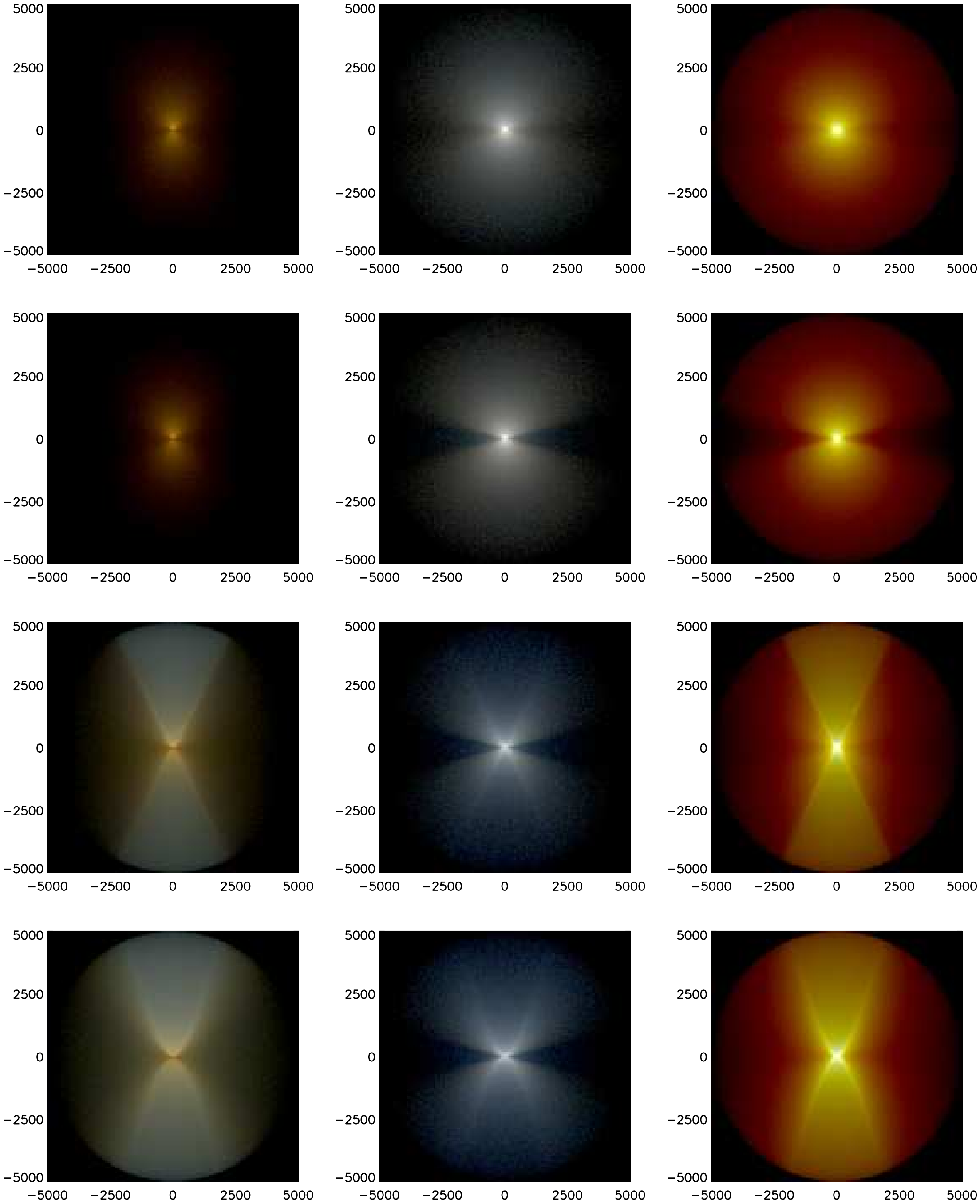

FIG. 8.— Three-color composite images of the four models (going from top to bottom) in three different wavelength regions (left to right), viewed at an inclination $i = 80°$. The near-IR images (left) are composites of images calculated through three NICMOS filters centered at 1.1, 1.6 and 2.05 μm. The mid-IR images (middle) are composites at three SIRTF IRAC filters centered at 3.6, 4.5, and 5.8 μm. And the far-IR images (right) are for the SIRTF MIPS filters centered at 24, 70 and 160 μm. The images are scaled logarithmically with minimum intensities of 0.01, 0.0074, and 0.5 MJy/sr for the near-IR, mid-IR, and far-IR images, respectively, assuming a distance of 140 pc.

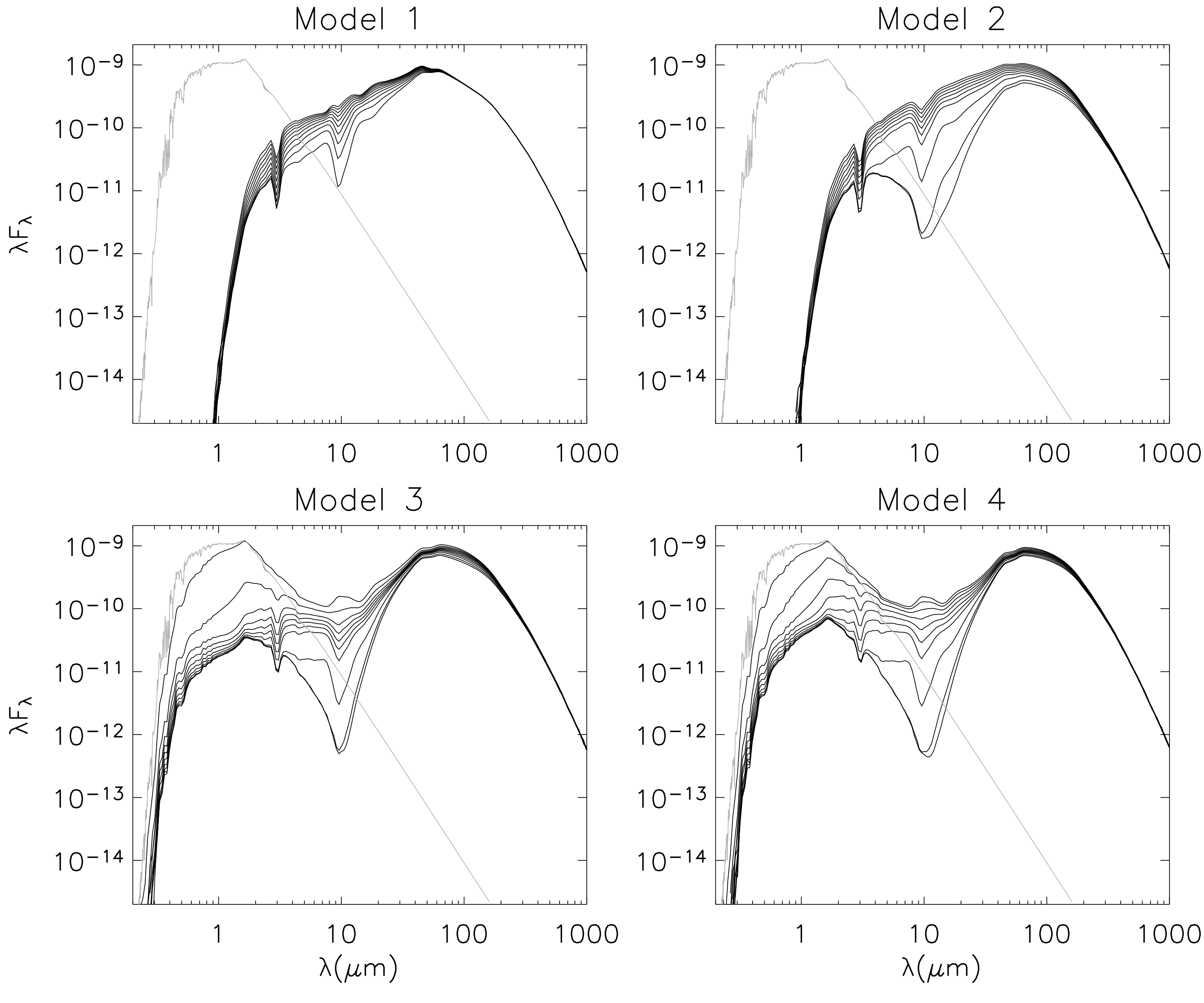

FIG. 9.— Spectral energy distributions for the four geometries. Fluxes (erg cm^{-2} s^{-1}) are scaled to a 1 $L_\odot$ source at a distance of 140 pc. Ten inclinations are plotted ranging from $\cos i = 0.05$ to 0.95 at intervals of 0.1. The light grey line is the input stellar spectrum.

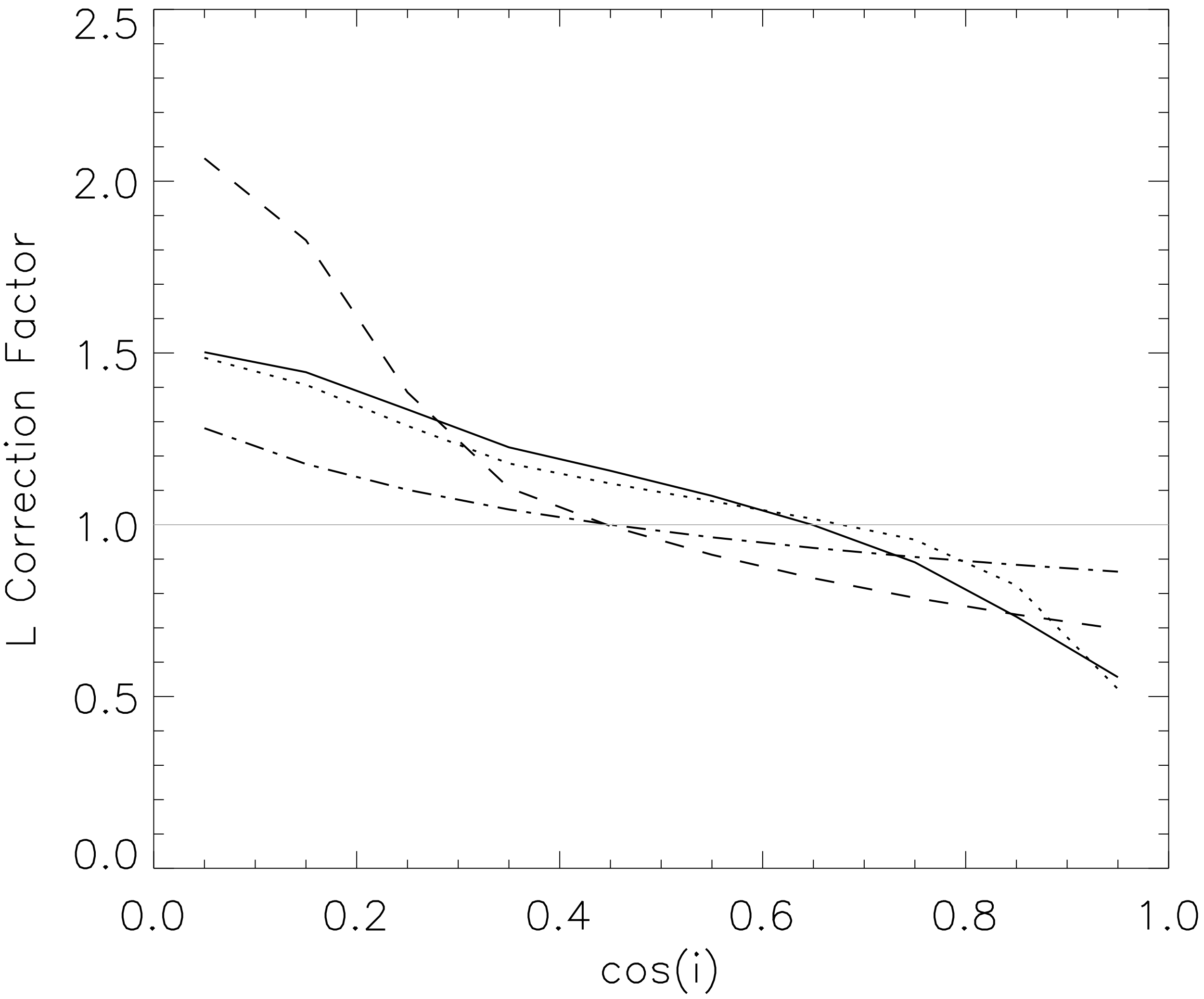

Fig. 10.— Luminosity correction factors as a function of inclination for the four geometries: Model 1: dot-dashed; Model 2: dashed; Model 3: dotted; Model 4: solid. These curves show the correction factor that would have to be applied to the integrated SED at a given inclination to correctly determine the source luminosity.

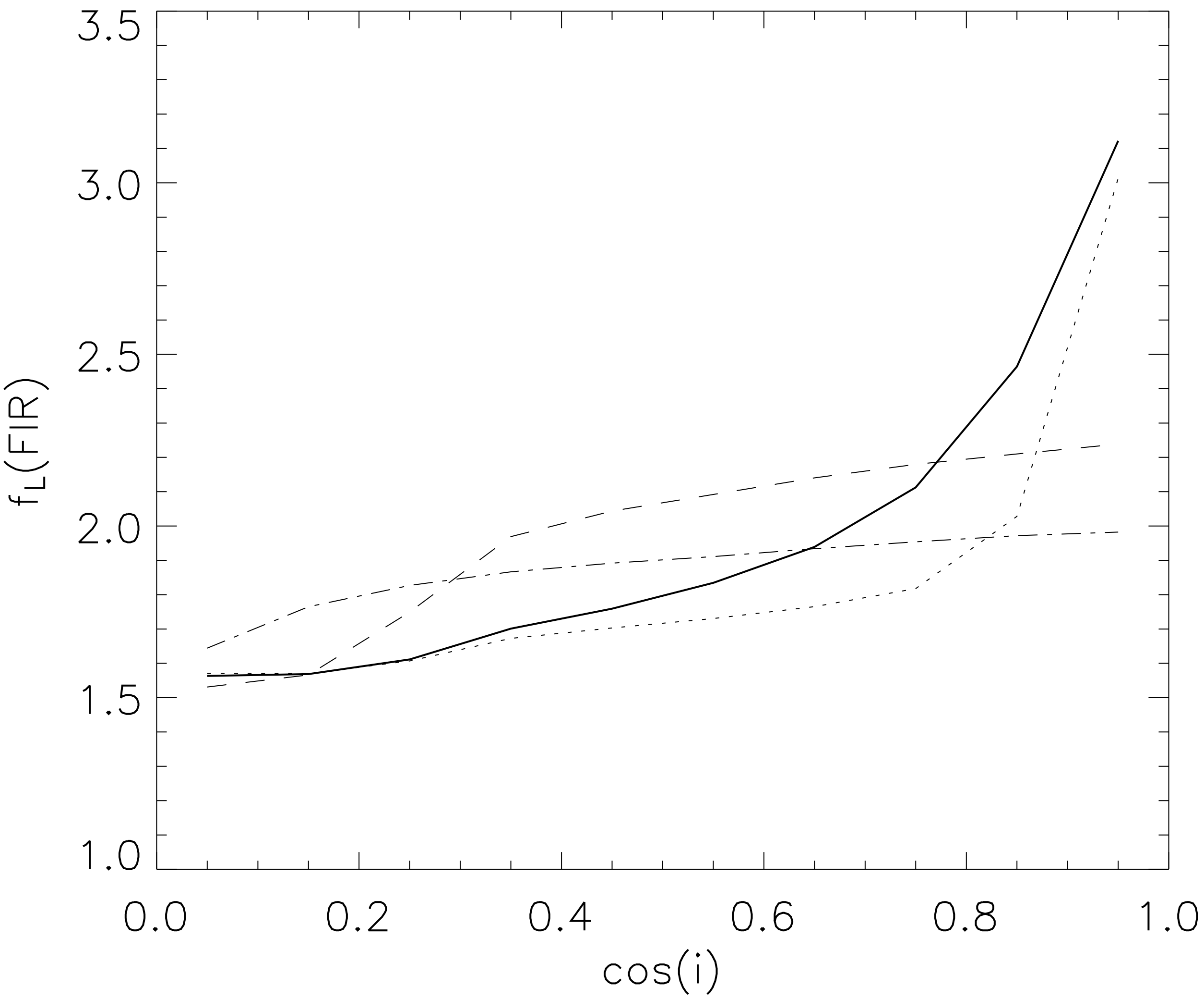

Fig. 11.— The ratio of the integrated SED to the maximum far-IR flux is plotted against inclination. Model 1: dot-dashed; Model 2: dashed; Model 3: dotted; Model 4: solid.

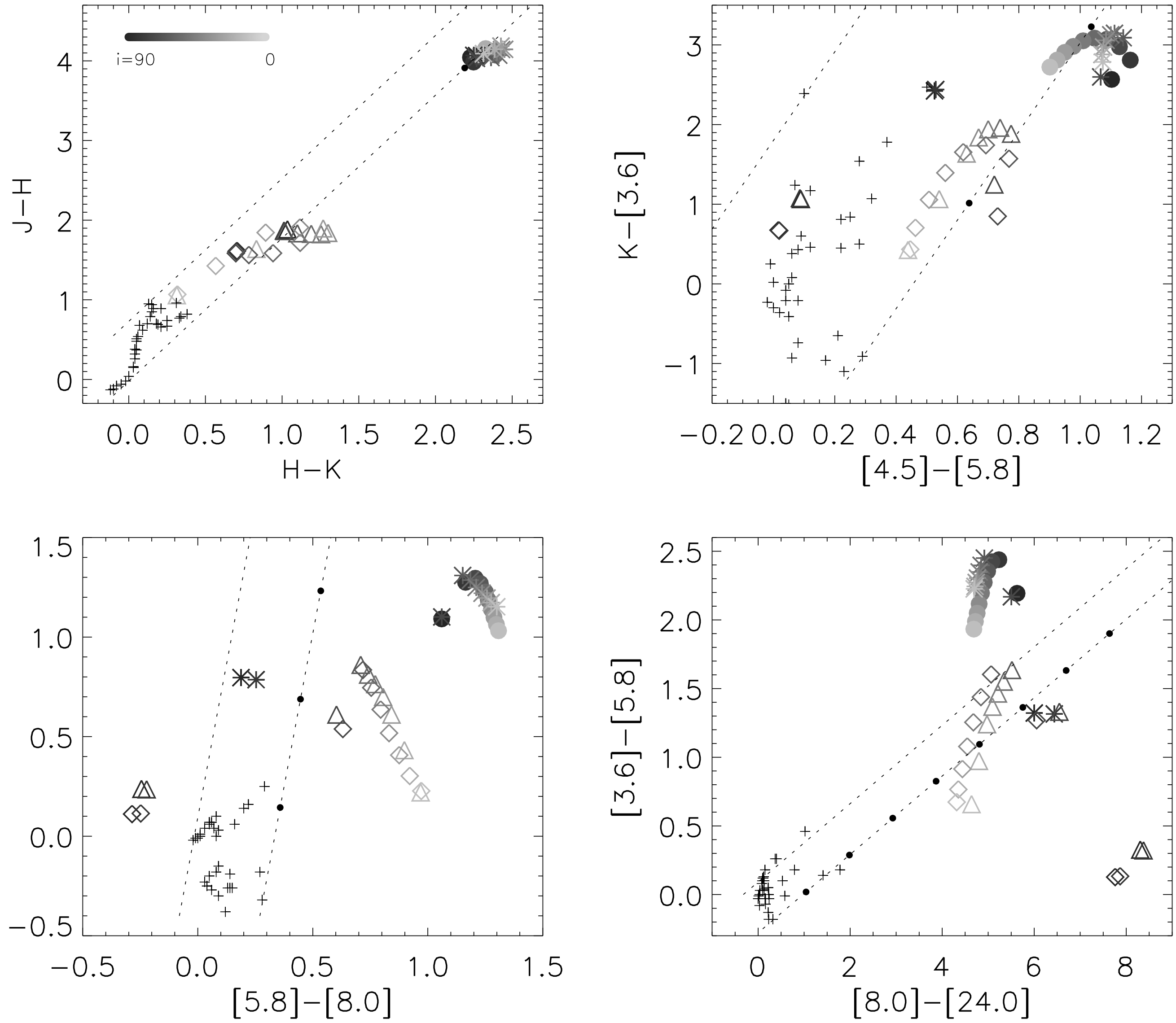

FIG. 12.— Color-color plots. The symbols correspond to the four models as follows, Model 1: filled circles; Model 2: asterisks; Model 3: open triangles; Model 4: open diamonds. The models with cavities (3 & 4) are much bluer than the models without (1 & 2), despite their similar envelope masses (Table 2). The symbols are plotted at different levels of greyscale to indicate inclination, as shown by the greyscale bar in the top left panel. Edge-on sources are black, and pole-on are light grey. Notice that some of the bluest sources are edge-on. This is due to the dominant contribution of scattered light to the source flux. These edge-on sources are very faint so would stand out in a color-magnitude diagram as faint and blue. The dotted lines are reddening vectors off the main sequence and red giant branch (small crosses). The black dots along one of the reddening lines denote increments of $A_V = 30$. The models in the bottom left panel are well-separated from reddened main sequence and giant stars. The models at bottom right are well-separated from stars with A_V less than 100.

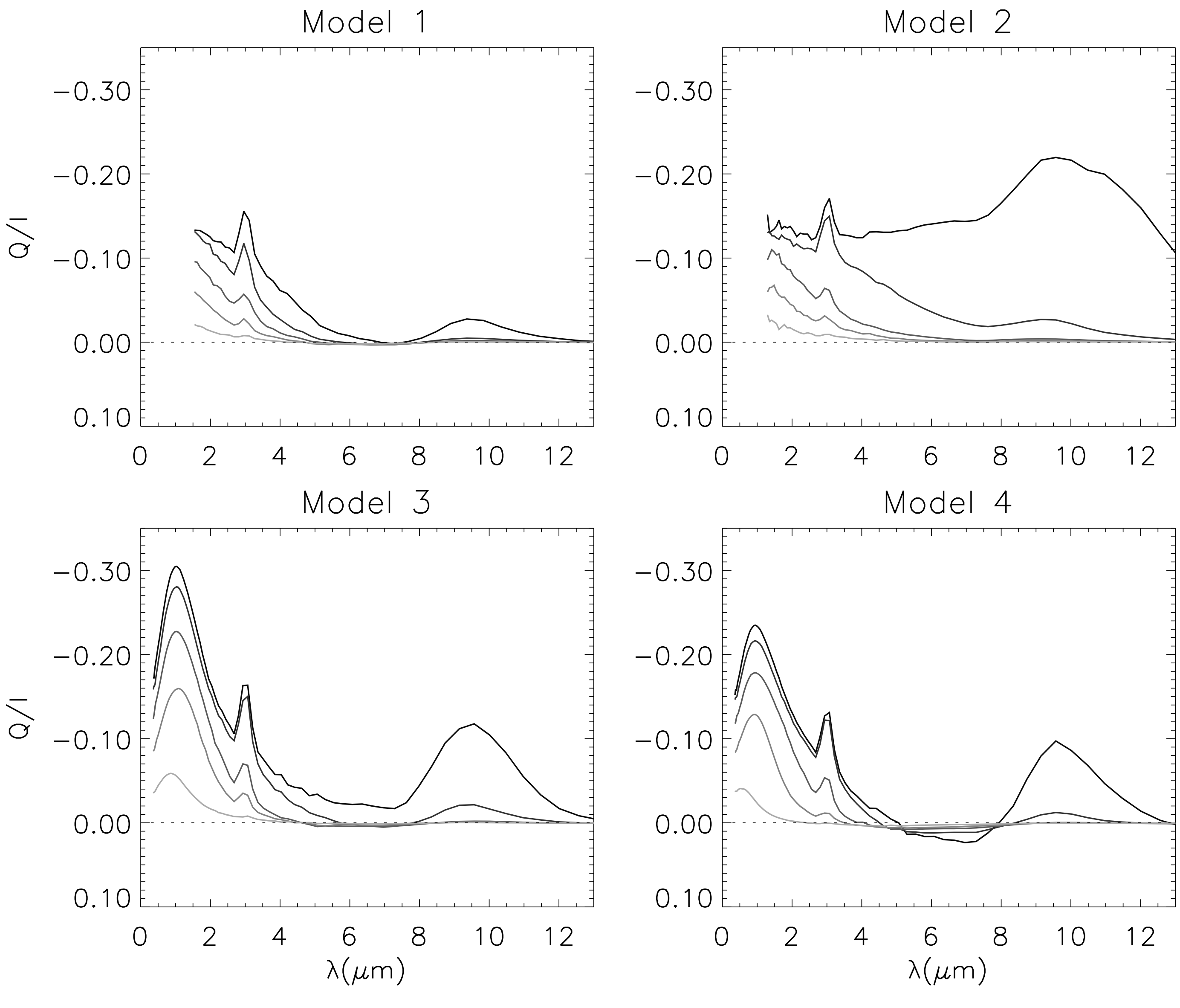

FIG. 13.— Polarization spectra for the four geometries. Five inclinations are plotted from $\cos i = 0.05$ to 0.85 in intervals of 0.2. The lines are lighter at lower inclinations.